Bachelor's Thesis

The Future of ENSO in CMIP6 Models

Fiona Fix

November 6, 2020

B.Sc. Meteorology
MIN Faculty
Universität Hamburg

Topic of the thesis as it was registered:
The Future of ENSO in CMIP6 Models

Abstract

Understanding and predicting El Niño Southern Oscillation (ENSO) is of great interest in order to minimise social, environmental and economic risks in many parts of the world that are affected by this phenomenon. Therefore, this work aims to investigate future behaviour of ENSO in Coupled Model Intercomparison Project Phase 6 (CMIP6) models.

A total of 50 models of the CMIP6 1 percent CO2 experiment (in which CO_2 is increased by 1 % per year) are analysed and basic methods are used to find an overall trend in the ENSO-Index. To identify the influence of internal variability, the same analysis is done for a 68-member ensemble of the MPI-ESM-LR model, which was run with different initial conditions. Furthermore, Linear Inverse Models (LIMs) are fitted to the single members as well as to the complete ensemble of the MPI-ESM-LR model, to find out whether LIMs fitted to single realisations deliver results that are representative for the entire ensemble.

As a result, it was found that the simple methods used do not capture any profound change in ENSO behaviour. The LIMs fitted to single realisations prove not to be representative for the entire ensemble, but the fit to the ensemble delivers promising results. They indicate that ENSO frequency decreases in a warming climate.

Contents

1 Introduction

El Niño Southern Oscillation (ENSO) is a coupled atmosphere-ocean oscillation in the tropical Pacific. It is characterised by warm and cold sea surface temperature (SST) anomalies in the eastern equatorial Pacific (Cai et al., 2015a; Kim et al., 2014; McPhaden et al., 2006; Kraus, 2004), which typically occur every 3 to 7 years (McPhaden et al., 2006; Berner et al., 2020; Kraus, 2004). Usually, warm water accumulates in the western Pacific because of the easterly trade winds, while upwelling brings colder water to the west coast of South America (Kraus, 2004). During a La Niña (LN) event this circulation strengthens, whereas during El Niño (EN) it is weakened or even reversed. Warm water drifts from the western to the central and eastern Pacific, where anomalously warm SSTs occur (McPhaden et al., 2006; Cai et al., 2015a; Kim et al., 2014; Kraus, 2004).

SST anomalies due to ENSO have an effect on atmospheric convection which drives teleconnections (Cai et al., 2015a). Due to these atmospheric teleconnections ENSO affects weather conditions worldwide (Cai et al., 2015a; Lin et al., 2018; Kraus, 2004) and is therefore one of the most important climate variations on an inter-annual time-scale. Strong EN events can for example, cause severe droughts in eastern Australia and floods in southern America (Cai et al., 2015a; McPhaden et al., 2006). The same processes also have an effect on Rossby waves, which is why they also affect weather conditions in higher latitudes. The resulting extreme weather events have a great impact on ecosystems and agriculture (Cai et al., 2015a). In order to reduce the social, environmental, and economic risks of those events, accurate forecasting is required. Therefore, understanding and predicting ENSO mechanisms is a central question of current research. In particular, the question of how ENSO will react to global warming is of great interest.

If and how ENSO behaviour will change under a changing climate has been studied intensively over the past years. The analyses of many different datasets with many different methods have resulted in different and often contradicting conclusions (Vecchi and Wittenberg, 2010). Even though climate models agree on the tendency of the climate's mean state, there is not so much consistency in the projections of ENSO properties (Guilyardi et al., 2009; Berner et al., 2020; Vecchi and Wittenberg, 2010). While McPhaden et al. (2006) state that there is no sign for a significant change in ENSO behaviour under increasing CO_2 scenarios, Cai et al. (2014, 2015b) conclude that as a result of changes in the mean state both extreme ENs and LNs become considerably more frequent. However, this has not been reviewed yet for many members of the newest generation of climate models (participating in Coupled Model Intercomparison Project Phase 6 (CMIP6)).

Berner et al. (2020) recently investigated the change in ENSO properties predicted by the large ensemble simulations of NCAR's Community Earth System Model, version 1. Kestin et al. (1998) indicated that ENSO could be a linear oscillator driven by stochastic forcing, and Penland and Sardeshmukh (1995) have shown that tropical SSTs can be modelled adequately by using Linear Inverse Models (LIMs). Based on this, Berner et al. (2020) used LIM simulations to increase the statistical reliability of their results (a similar approach has been used by Capotondi and Sardeshmukh (2017)). This method could open the possibility to derive statistically robust results from small ensembles or even single realisations. The predictions of different climate models could potentially be compared more easily if the method is applied to the single members

of a multi-model ensemble like in CMIP6. However, in order to use the method for the members of the CMIP6-ensemble, it would have to be shown that the method is valid and robust if the LIM is fitted only to a single ensemble member instead of to a whole ensemble of the given model.

Therefore, this work aims to answer two central questions: Do CMIP6 models predict changes in ENSO properties and do LIMs fitted to single climate model realisations yield robust and reliable results? To answer these questions, I use three different simple approaches to determine whether the climate models participating in CMIP6 predict future changes in ENSO behaviour. An ENSO-Index based on SST-anomalies is chosen as a measure of ENSO activity. The moving average of the ENSO-Index can be useful to identify overall trends in the index. Additionally, I calculated the standard deviation of the ENSO-Index over 30-year moving windows. The third simple approach is supposed to detect changes in periodicity by counting ENSO-events. The analysis of these three simple methods shows no indication that there is a change in ENSO behaviour predicted by the CMIP6 models.

Since changes are expected to be quite subtle, a more sophisticated and more sensitive method might come to a different result. Therefore, I additionally use LIM simulations to find changes in ENSO periodicity. I test the accuracy/suitability of this method by fitting LIMs to a complete ensemble of the MPI-ESM-LR model, as well as to each single member of this ensemble. The results from the LIMs fitted to single realisations differ substantially so they are not representative for the entire ensemble. The results gained from the LIM fitted to the complete ensemble seem to show a trend towards longer periods, but further analysis is necessary to determine whether this trend is actually statistically significant.

This work is structured as follows. In chapter 2 the climate model ensembles used in this work are introduced and the index used for ENSO description is explained. The methodology chapter (3) is divided in three sections. I start by describing the simple methods used to identify changes in ENSO behaviour in section 3.1, before explaining the more sophisticated method of LIM in section 3.2. In section 3.3 a simple example is given to illustrate the method. Results are given and discussed in chapter 4 before a summary and outlook is given in chapter 5.

2 Data

2.1 Ensembles

This work makes use of two different climate model ensembles which both ran simulations for the 1 percent CO_2 (1pctCO2) experiment: (a) a multi-model ensemble contributing to CMIP6 and (b) an initial conditions ensemble from the MPI-ESM-LR model. The 1pctCO2 experiment is one of the Diagnostic, Evaluation and Characterization of Klima (DECK) experiments of the Coupled Model Intercomparison Project (CMIP), which were defined to ensure consistency between the phases of CMIP (WCRP , 2020). The 1pctCO2 experiment is an idealised experiment which is initialized from the pre-industrial control simulation (piControl). A 150-year period is simulated. The CO_2 concentration is increased by $1\dot{\%}$ per year which results in a doubling after 70 and a quadrupling after 140 years, respectively (Giorgetta et al., 2013).

In this work properties of ENSO shall be investigated in CMIP6 models. I use an ensemble of 50 General Circulation Models (GCMs) participating in the CMIP6 1pctCO2 experiment. This ensemble will be referred to as the CMIP6-ensemble. A list with detailed information can be found in table 1. Because different models have different spatial resolution, different implementation or parametrisation of physical and chemical processes, simulations differ sometimes substantially. Using a multi-model ensemble, such as the CMIP6-ensemble allows the estimation of the uncertainty caused by these differences. Forecasts can be improved by using multi-model ensembles instead of single simulations because by using such an ensemble the most likely future state of the atmosphere can be predicted. The spread between the models then corresponds to the uncertainty of the forecast (UK Met Office , 2020).

The uncertainty due to differences in the model realisation is not the only uncertainty in such ensembles. Because of the chaotic nature of the climate system, the slightest differences in the model's initial conditions can result in very different model outcomes (UK Met Office , 2020; Deser et al., 2020). By using so called initial conditions ensembles, the signal caused by this internal climate variability can be identified. These ensembles consist of different realisations of the same model run with different initial conditions (UK Met Office , 2020; Deser et al., 2020). To identify the internal variability as well as for method testing and comparison, a second ensemble is used in this work. The MPI-ESM-LR model has been run for the 1pctCO2 experiment with slightly different initial conditions which results in a 68-member ensemble (Plesca et al., 2017; Giorgetta et al., 2013; Stevens et al., 2013). This ensemble will from now on be referred to as MPI-ensemble. It should be mentioned that this ensemble is older than the CMIP6 one, since it was run for the Coupled Model Intercomparison Project Phase 5 (CMIP5). The reason for using an older ensemble for this work was the availability of this dataset.

Table 1: Details of the CMIP6 climate models

No.	Model	Variant	Version	Horizontal Grid lat x lon	Institution	Reference
1	ACCESS-CM2	r1i1p1f1	v20191109	300x360	Commonwealth Scientific and Industrial Research Organisation, Australian Research Council Centre of Excellence for Climate System Science, Australia	Dix et al. (2019)
2	ACCESS-ESM1-5	r1i1p1f1	v20191115	300x360		Ziehn et al. (2019)
3	AWI-CM-1-1-MR	r1i1p1f1	v20181218	unstructured, 830305 wet nodes	Alfred Wegener Institute, Helmholtz Centre for Polar and Marine Research, Germany	Semmler et al. (2018)
4	BCC-CSM2-MR	r1i1p1f1	v20181015	232x360	Beijing Climate Center, China	Wu et al. (2018)
5	BCC-ESM1	r1i1p1f1	v20190611	232x360		Zhang et al. (2019)
6	CAMS-CSM1-0	r1i1p1f1	v20190708	200x360	Chinese Academy of Meteorological Sciences, China	Rong (2019a)
7	CAMS-CSM1-0	r2i1p1f1	v20190726	200x360		Rong (2019b)
8	CESM2-WACCM	r1i1p1f1	v20190425	384x320	National Center for Atmospheric Research, USA	Danabasoglu (2019b)
9	CESM2	r1i1p1f1	v20190425	384x320		Danabasoglu (2019a)
10	CNRM-CM6-1-HR	r1i1p1f2	v20191021	1050x1442	Centre National de Recherches Meteorologiques and Centre Europeen de Recherche et de Formation Avancee en Calcul Scientifique, France	Voldoire (2019)
11	CNRM-CM6-1	r1i1p1f1	v20180626	294x362		Voldoire (2018)
12	CNRM-ESM2-1	r1i1p1f2	v20181018	294x362		Seferian (2018a)
13	CNRM-ESM2-1	r2i1p1f2	v20181031	294x362		Seferian (2018b)
14	CNRM-ESM2-1	r3i1p1f2	v20181107	294x362		Seferian (2018c)
15	CNRM-ESM2-1	r4i1p1f2	v20190328	294x362		Seferian (2018d)
16	CanESM5	r1i1p1f1	v20190429	291x360*	Canadian Centre for Climate Modelling and Analysis, Environment and Climate Change Canada, Canada	Swart et al. (2019)
17	CanESM5	r1i1p2f1	v20190429	291x360*		
28	CanESM5	r2i1p1f1	v20190429	291x360*		
19	CanESM5	r2i1p2f1	v20190429	291x360*		
20	CanESM5	r3i1p1f1	v20190429	291x360*		
21	CanESM5	r3i1p2f1	v20190429	291x360*		
22	E3SM-1-0	r1i1p1f1	v20191008	180x360*	Lawrence Livermore National Laboratory, Argonne National Laboratory, Brookhaven National Laboratory, Los Alamos National Laboratory, Lawrence Berkeley National Laboratory, Oak Ridge National Laboratory, Pacific Northwest National Laboratory, Sandia National Laboratories, USA	Bader et al. (2019)
23	EC-Earth3-Veg	r1i1p1f1	v20190702	292x362	EC-Earth consortium	EC-Earth (2019)
24	GFDL-CM4	r1i1p1f1	v20180701	1080x1440	National Oceanic and Atmospheric Administration, Geophysical Fluid Dynamics Laboratory, USA	Guo et al. (2018)
25	GFDL-ESM4	r1i1p1f1	v20180701	576x720		Krasting et al. (2018)
26	GISS-E2-1-G	r102i1p1f1	v20190815	90x144*	NASA Goddard Institute for Space Studies, USA	NASA/GISS (2018a)
27	GISS-E2-1-G	r1i1p1f1	v20180905	90x144*		NASA/GISS (2018b)
28	GISS-E2-1-G	r1i1p3f1	v20190702	90x144*		NASA/GISS (2018c)
29	GISS-E2-1-H	r1i1p1f1	v20190403	90x144*		NASA/GISS (2019a)
30	GISS-E2-2-G	r1i1p1f1	v20191120	90x144*		NASA/GISS (2019b)
31	HadGEM3-GC31-LL	r1i1p1f3	v20190620	330x360	Met Office Hadley Centre, United Kingdom	Ridley et al. (2019a)
32	HadGEM3-GC31-LL	r2i1p1f3	v20190724	330x360		Ridley et al. (2019b)
33	HadGEM3-GC31-LL	r3i1p1f3	v20190821	330x360		Ridley et al. (2019c)
34	HadGEM3-GC31-LL	r4i1p1f3	v20190821	330x360		
35	INM-CM4-8	r1i1p1f1	v20190530	180x360*	Institute for Numerical Mathematics, Russia	Volodin et al. (2019)
36	IPSL-CM6A-LR	r1i1p1f1	v20180727	332x362	Institut Pierre Simon Laplace, France	Boucher et al. (2018)
37	MCM-UA-1-0	r1i1p1f1	v20190731	80x192	Department of Geosciences, University of Arizona, USA	Stouffer (2019)

to be continued on the next page

No.	Model	Variant	Version	Horizontal Grid lat x lon	Institution	Reference
38	MIROC-ES2L	r1i1p1f2	v20190823	265x360	Japan Agency for Marine-Earth Science and Technology, Atmosphere and Ocean Research Institute, The University of Tokyo, National Institute for Environmental Studies, RIKEN Center for Computational Science, Japan	Hajima et al. (2019)
39	MIROC6	r1i1p1f1	v20181212	265x360		Tatebe and Watanabe (2018)
40	MPI-ESM1-2-HR	r1i1p1f1	v20190710	404x802	Max Planck Institute for Meteorology, Germany	Jungclaus et al. (2019)
41	MPI-ESM1-2-LR	r1i1p1f1	v20190710	220x256		Wieners et al. (2019)
42	MRI-ESM2-0	r1i1p1f1	v20190904	363x360*	Meteorological Research Institute, Japan	Yukimoto et al. (2019)
43	NESM3	r1i1p1f1	v20190703	292x362*	Nanjing University of Information Science and Technology, China	Cao and Wang (2019)
44	NorCPM1	r1i1p1f1	v20190914	384x320	NorESM Climate modeling Consortium, Norway	Bethke et al. (2019)
45	NorESM2-LM	r1i1p1f1	v20190815	385x360*		Seland et al. (2019)
46	SAM0-UNICON	r1i1p1f1	v20190323	384x320	Seoul National University, Republic of Korea	Park and Shin (2019)
47	UKESM1-0-LL	r1i1p1f2	v20190701	330x360	Met Office Hadley Centre, United Kingdom	Tang et al. (2019a)
48	UKESM1-0-LL	r2i1p1f2	v20191009	330x360		Tang et al. (2019b)
49	UKESM1-0-LL	r3i1p1f2	v20190604	330x360		Tang et al. (2019c)
50	UKESM1-0-LL	r4i1p1f2	v20190604	330x360		

*values for the horizontal grid differ between the NetCDF file header and/or the reference given in the header and/or the dimensions of the array that could be read in. The values given here are the dimensions of the arrays read in with python's netCDF4 Dataset function.

2.2 ENSO-Index

In order to measure ENSO activity, several indices have been introduced, each with their own advantages and disadvantages. Therefore, depending on the problem and the available data, different indices have proven to be helpful. One scalar quantity defined by the NOAA Climate Prediction Center, National Weather Service (NOAA CPC) (2020b) is the Ocean Niño Index (ONI). It is calculated from monthly SSTs in the Nino3.4 region, which is located at 5°N -5°S and 120°-170°W (see Figure 1, NOAA CPC (2020b)). First, SST anomalies have to be calculated for each grid-point. To account for the warming trend in the region, this is done with respect to a centred 30-year base-period, which is updated every five years. The base-period corresponding to the years x to x+5 is the period x-15 to x+15 (NOAA CPC , 2020a). Second, the 3-month-running mean of these anomalies has to be calculated. The ONI is then defined as the field mean of the Nino3.4 region of those smoothed anomalies (NOAA CPC , 2020b).

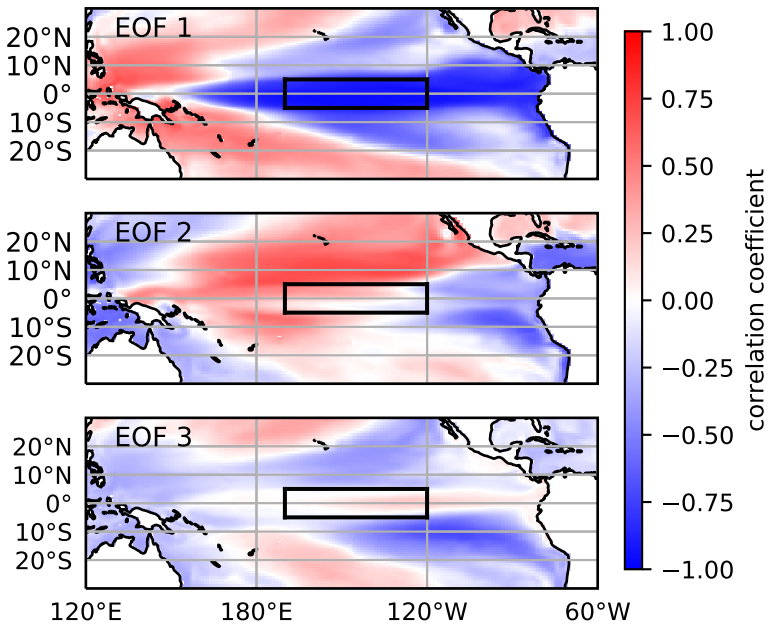

Figure 1: Map of the equatorial Pacific. The Nino3.4 region is marked with a black box. The patterns of empirical orthogonal function (EOF) 1, 2 and 3 are displayed in colour (model: ACCESS-CM2).

This method, however, creates problems at the beginning and the end of a dataset. For the first and last 15 years there is no centred base-period available, so the first (last) 30-year base-period has to be used for the first (last) 20 years. This means that the anomalies of the first (last) 15 years are calculated with respect to a non-centred base-period, which, due to global warming, is warmer (cooler) than the correct base-period would have been. The anomalies therefore appear to be smaller (bigger) than they actually are, which creates an apparent trend in the time series of the ONI. Therefore, the first and last 15 years of data can not be correctly evaluated and will not be taken into account for the following analysis.

The NOAA CPC (2020b) defines conditions which are considered EN- or LN-like as well as EN- and LN-events. When the ONI is $>0.5\,\mathrm{K}$ or $<0.5\,\mathrm{K}$, the conditions are considered EN- or LN-like, respectively. Whenever this happens for 5 consecutive months, it is called an EN-/LN-event.

Another way to define an ENSO-Index is by using the principle component (PC) of the first empirical orthogonal function (EOF) of equatorial monthly SST anomalies (Berner et al., 2020; Penland and Sardeshmukh, 1995). The pattern of the first EOF explains most of the variability in the tropical Pacific, particularly in the Nino3.4 region (see Figure 1, Dommenget et al. (2013)). The index is based on SST data from the tropical Pacific (120°E-60°W, 30°N-30°S). To eliminate the climate trend and the annual cycle, anomalies are calculated for each grid-point with respect to a centred base-period as described above. Subsequently, they are smoothed by a 3-month-running mean. From these smoothed anomalies the EOFs can be calculated, yielding the patterns as well as the time series of the PCs. The first PC is used as an ENSO-Index and will from now on be referred to as PC-Index. The advantage of this index is that, together with the higher PCs, it describes the properties of SST variation more accurately than others. It can therefore be used for further analysis (see section 3.2), which is why I chose this index for my investigations.

It can be shown that ONI and PC-Index are highly correlated, which means that they indeed describe the same ENSO variations. For the 50-member ensemble of the CMIP 1pctCO2 experiment the correlation of the two indices lies between 0.869 and 0.994 with an ensemble mean of 0.981. To show this in an example, the time series of both indices are shown for five arbitrarily selected ensemble members in figure 2.

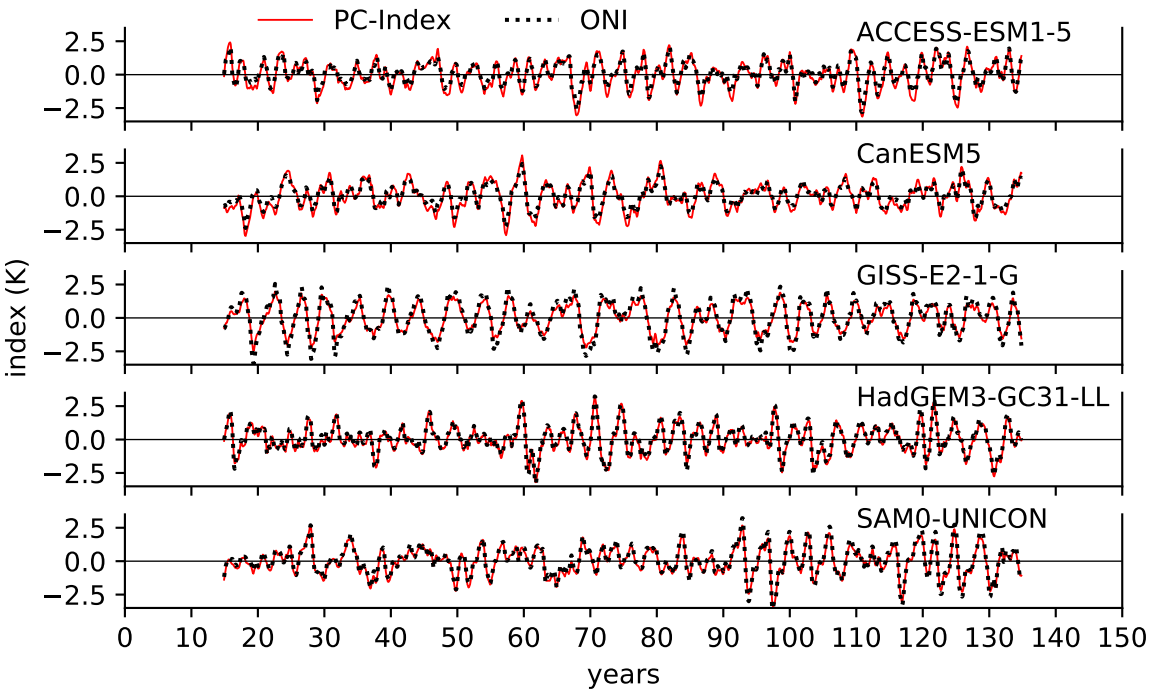

Figure 2: Time series of ONI (black, dotted) and PC-Index (red, solid) for five arbitrarily chosen ensemble members (ACCESS-ESM1-5,CanESM5,GISS-E2-1-G,HadGEM3-GC31-LL, SAM0-UNICON, compare table 1).

3 Methodology

3.1 Simple Approaches

In the beginning, I choose three very simple approaches to determine if ENSO behaviour is projected to change in a changing climate.

In order to determine whether the SST fluctuations caused by ENSO underlie an overall trend, a 30-year moving average (MA) was calculated. When a MA is applied, fluctuations are smoothed and therefore longer term trends in time series can be detected. By calculating a MA periodical fluctuations in particular are eliminated. Therefore, this method can only pick up overall trends in the time series. It might be able to pick up increases or decreases of amplitude or frequency, if they change more (or less) for positive than for negative values. The length of the time window over which the average is build has to be chosen according to the data. In this case the window has to be long enough for the method to pick up climate trends but not shorter variabilities. On the other hand it has to be short enough, so that a meaningful time series can be generated by moving the window. Thirty years therefore seem to be a good compromise. If I_i is the PC-Index at time-step i then the MA at time-step t is defined as:

$$MA_t = \frac{1}{(30 \cdot 12)} \sum_{t-(15 \cdot 12)}^{t+(14 \cdot 12)} I_i \tag{1}$$

The multiplication by 12 is due to the fact that monthly data is used.

If both EN- and LN-events become stronger (weaker) and/or more (less) frequent, this would not necessarily show up as a trend in the moving average, but it would manifest in an increasing (decreasing) standard deviation. Therefore the standard deviation is calculated for a 30-year moving window. It could, however, be the case that for example the frequency of the oscillation increases while the amplitude decreases. So, there would be two major changes, which together would have a compensating effect on the standard deviation and therefore might go undetected by the method.

Cai et al. (2014 and 2015b) analysed models from CMIP phases 3 and 5 and suggested that, due to a warmer base state, both EN and LN events will occur considerably more often in the future. To check whether a change in ENSO frequency is detectable in the CMIP6 models, a third simple approach is introduced. I counted the number of ENSO-events in a 30-year period, to see whether the number increases for later periods. I considered the number of months with EN-/LN-like conditions, as well as the number of events, where the threshold (of ± 0.5K) was exceeded for at least 5 consecutive months.

3.2 Linear Inverse Model

Berner et al. (2020) used Linear Inverse Models (LIMs) to increase the statistical confidence of their results when using PCs to analyse ENSO behaviour. The question arises whether this approach is also applicable to single members of an ensemble. Therefore, I compare results derived from fitting LIMs to the complete MPI-ensemble to results gained from fitting LIMs to single members of that same ensemble.

A pattern at the time $t + \tau$ can be predicted from a pattern at the time t, if a system is assumed to be linear and markovian (Penland, 1989). Penland (1989) expects the LIM to be useful for longer-range prediction, but it is required that non-linear effects have to be slow with respect to the sampling rate. Any dynamical system that meets these conditions can be described as (Penland, 1989; Penland and Sardeshmukh, 1995):

$$d\hat{x}/dt = B\hat{x} + n(\hat{x}) + f \tag{2}$$

In this equation $\hat{x}$ is the state vector, B the linear feedback matrix and n and f are non-linear and external forcing terms. Penland and Sardeshmukh (1995) show that tropical SSTs can be described by the N-dimensional Markov process:

$$dx/dt = Lx + \xi \tag{3}$$

where x is the new state vector containing only the variables of the subsystem of interest (SSTs in this case), L is the new feedback matrix (a submatrix of B), and ξ is a white noise forcing. This does not mean that the non-linear forcing terms in equation 2 are neglected, but rather that they can be described by a linear process and white noise (Penland, 1989; Penland and Sardeshmukh, 1995). The process is considered to be continuous and discretely sampled rather than an intrinsically discrete process (Penland, 1989).

In order to determine a pattern at time $t + \tau$ from the pattern at the time t one has to integrate equation 3, which results in:

$$x(t + \tau) = exp(L\tau)x(t) + \zeta(t, \tau) = G(\tau)x(t) + Sr \tag{4}$$

For simplicity, the Green-function $G(\tau)$ is introduced. The noise $\zeta = Sr$ is white. A LIM is a N-dimensional Markov process (like equation 3), in which one determines the feedback matrix L (or G) of the system from (observational) data (Newman et al., 2009), as well as the properties of the noise ζ. It can be useful to do this in EOF space, because by choosing a certain number of PCs the dimensionality can easily be reduced, and the covariance matrix C_0 of x becomes diagonal (Penland, 1989). If x is N-dimensional (e.g a time-series of the first N PCs), L is the constant NxN feedback matrix. The covariance matrix (denoted with angle brackets $\langle\rangle$) and lag-covariance matrix of the vector x are defined as (Penland, 1989; Newman et al., 2009; Penland and Sardeshmukh, 1995):

$$\langle x(t)x^T(t)\rangle = C_0 \tag{5}$$

$$\langle x(t + \tau)x^T(t)\rangle = C_\tau \tag{6}$$

x^T is the transposed of x. The covariance matrix Q of the noise ξ is constant (Penland, 1989; Penland and Sardeshmukh, 1995):

$$\langle \xi\xi^T \rangle = Q \tag{7}$$

The transition probability of the stochastic differential equation (3) is described by a Fokker-Planck-equation, from which (after some mathematical manipulations and integration) follows

an equation for Q (Penland, 1989; Penland and Sardeshmukh, 1995):

$$LC_0 + C_0L^T + Q = 0 \tag{8}$$
$$Q = -LC_0 - C_0L^T \tag{9}$$

By manipulating the Fokker-Planck equation again, and solving the resulting differential equation, the following relation between C_0, C_τ and $G(\tau)$ is found (Penland, 1989; Penland and Sardeshmukh, 1995; Berner et al., 2020):

$$C_\tau = G(\tau)C_0 \tag{10}$$
$$G(\tau) = C_\tau C_0^{-1} \tag{11}$$

With equations 11, 5 and 6, $G(\tau)$ or L can be calculated from the data. The noise ζ in equation 4 is white with covariance $E = SS^T$, so $\zeta = Sr$, where r is a normally distributed random vector. Penland (1989) shows that E can be calculated from the data (see also Newman et al. (2009)):

$$E = \langle \zeta\zeta^T \rangle = C_0 - G(\tau)C_0G^T(\tau) = SS^T \tag{12}$$

From equation 12, S can be deduced by means of the Cholesky matrix decomposition. For the system to be stationary, G is required to tend to zero for long lags τ and therefore the covariance matrix of the noise tends to the covariance matrix of x itself (Penland, 1989).

Overall, in order to fit a LIM to a given SST time series (of one ensemble member), I take the following steps: First, I calculate the EOFs and PC time series. I use the eofs python package (Dawson, 2016) with the pc-scaling option 1 (scaled to unit-variance), because this yields the best compatibility with the ONI. Penland and Sardeshmukh (1995) argued that using the first 15 PC time series as x is a good compromise and they show that using 10 or 20 EOFs does not change the main results. Therefore, I choose the time series of the first 15 PCs to be the 15 components of x. Second, I calculate the covariance matrices of x as in equations 5 and 6. As a lag, I choose $\tau = 1$ month. Berner et al. (2020) expect that, if the approximation is valid, there should be several τ for which the LIM delivers accurate results. They show that for their application a range of τ from 1 to 12 months shows qualitatively similar results. This range lies between the limits of the time scale on which non-linearities become important and the time scale where sampling errors dominate (Berner et al., 2020).

With equations 11 and 12 G and E can be derived. Then, E needs to be decomposed to get S. The Cholesky matrix decomposition is only possible for positive-definite matrices, which can create problems if the noise is correlated. This is prevented here by setting all values in the covariance matrix E to zero except the elements of the main diagonal. S can then be calculated as $S = \sqrt{E}$. This manipulation can be made without changing the main properties of the model, because it only concerns the noise ζ. The feedback matrix L (and therefore G), which contains all the information about the oscillation, is not altered by this adjustment. Having derived G and S, I can now use equation 4 and different random vectors r to get as many realisations of the LIM as required.

To fit a LIM to the whole ensemble, I calculate the EOFs for the whole ensemble by stacking the SST time series of the single members. Then, I split the PC time series again, in order to calculate the covariance matrices for each member. Subsequently, those covariance matrices are averaged before calculating G and ultimately the LIM.

3.3 LIM: Example

In order to get a better understanding of the method and check the accuracy of my implementation, I calculated a simple case as an example. This example is supposed to be similar to actual SSTs but with known properties of the oscillation. I artificially generated a propagating wave of SST anomalies based on a damped linear oscillator forced by noise with the following properties:

$$d\mathbf{x}/dt = L\mathbf{x} + Ar \tag{13}$$

L is the linear feedback matrix given by

$$L = \begin{pmatrix} -\nu & \omega \\ -\omega & -\nu \end{pmatrix} \tag{14}$$

where the damping rate is $\nu = 0.01\,\text{month}^{-1}$ and the angular frequency $\omega = 2\pi/24\,\text{month}^{-1}$, respectively. The chosen noise forcing is uncorrelated with amplitude A:

$$\frac{A}{\text{K month}^{-1}} = \begin{pmatrix} 10 & 0 \\ 0 & 10 \end{pmatrix} \tag{15}$$

r is a random vector.

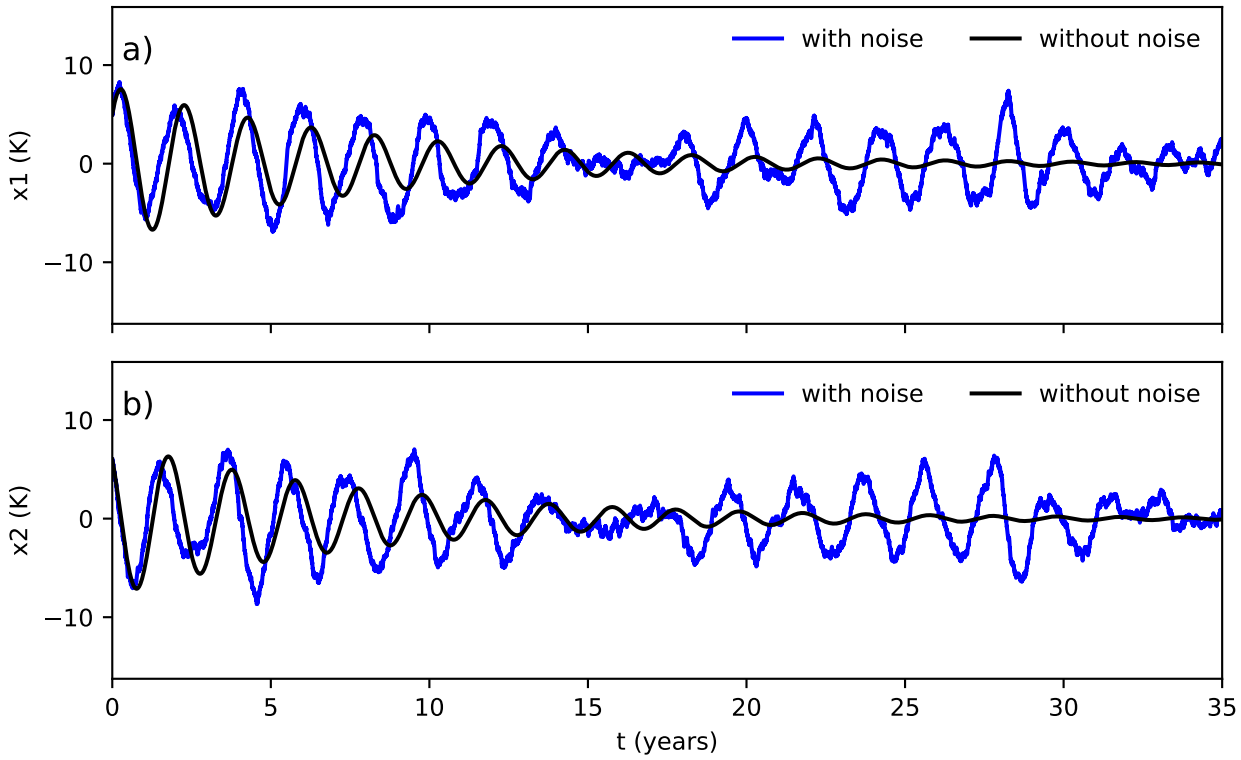

Figure 3: First 35 years of the time series of $\mathbf{x}$ (according to eq. 13-15) integrated with (blue) and without (black) noise. The two components of $\mathbf{x}$, $\mathbf{x1}$ (a) and $\mathbf{x2}$ (b), are plotted separately.

I integrated equation 13 over 10.000 months to receive a time series of the 2D state vector $\mathbf{x} = \binom{\mathbf{x_1}}{\mathbf{x_2}}$, which are two time series of temperatures. As visualised in figure 3, integration of

equation 13 without noise Ar results in a simple 2D damped oscillator, whereas if integrated including the noise the oscillator becomes forced and statistically stationary, although still with the same frequency and damping rate. Stationarity (of the statistical properties) is one major condition for the use of a LIM, so the noise is necessary for the method to be applicable to the example.

Now a dataset of artificially generated „SST-anomalies" with known damping rate ν and angular frequency ω can be created. I chose a xxy-field with 90x60 grid-points to illustrate this artificial data.

$$C(x, y, t) = (\mathbf{x_1}(t) \cdot cos(kx) - \mathbf{x_2}(t) \cdot sin(kx)) \cdot cos(ly) + N(\mu, \sigma) \tag{16}$$

with:

$$k = 2\pi/90 \tag{17}$$
$$l = 2\pi/60 \tag{18}$$
$$\mu = 0\,\mathrm{K} \tag{19}$$
$$\sigma = 2\,\mathrm{K}^2 \tag{20}$$

where k is the zonal wave number, l the meridional wave number, and N represents normally distributed noise with mean μ and variance σ. In figure 4, three time steps of the resulting dataset are displayed.

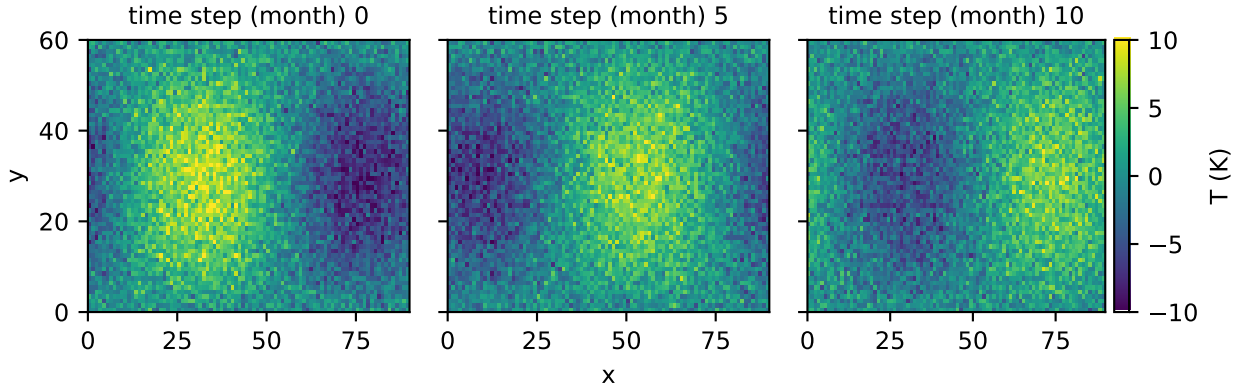

Figure 4: Three time steps of the artificially generated, propagating SST-anomaly wave in the xxy-grid

This is now a propagating but statistically stationary wave of artificial SST anomalies which can be modelled with a LIM. I calculated the PCs of the first 15 EOFs, the covariance matrices, G, E, S, and finally the LIM as described in 3.2. The time series of the first PC of the artificial data and five realisations of the LIM can be seen in figure 5. All the properties of the oscillation are captured in the eigenvalues ($\lambda_{1/2}$) of the feedback matrix L (Berner et al., 2020).

$$\lambda_{1/2} = -\nu \pm i\omega \tag{21}$$

Therefore, the real and imaginary parts of these eigenvalues indicate the e-folding time τ_d and the frequency f of the eigenmodes (Berner et al., 2020):

$$\tau_d = -1/\nu = 1/real(\lambda) \tag{22}$$
$$f = \omega/2\pi = \pm imag(\lambda)/2\pi \tag{23}$$

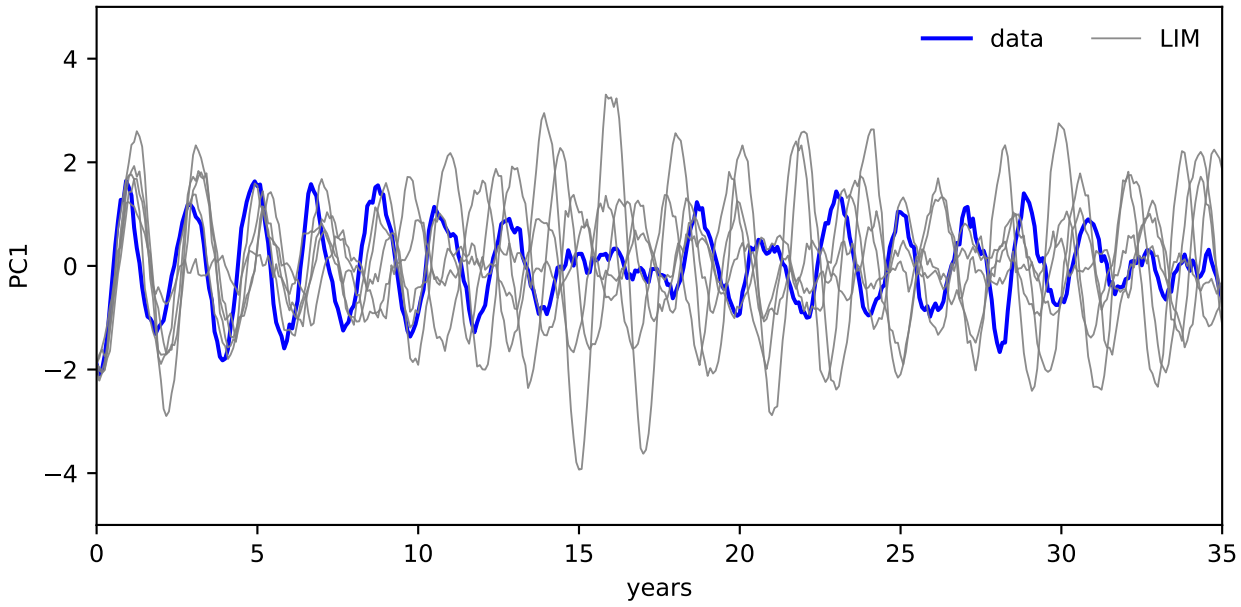

Figure 5: Time series of the first PC for the example data (blue) and 5 realisations of the LIM (grey).

Thus, one can easily identify dominant frequencies of the process. In figure 6 the e-folding times are plotted against the frequencies for the example from figure 5. Note that the feedback matrix L is the same for all realisations.

A different way to identify dominant frequencies is to look at the spectra of the time series. As suggested by Berner et al. (2020), the power spectral density (PSD) is computed directly from the Fourier coefficient of the time series using Welch's periodogram method (which is included in python's scipy.signal package). The Welch's periodograms for the data and the 5 realisations of the LIM are also plotted in figure 6.

It can be seen that there is a distinct peak in the Welch's periodogram of the data (denoted by the red vertical line). The LIMs show almost exactly the same peak position. At the same time, the eigenvalues of L show the longest e-folding time at almost exactly the same frequency. According to the eigenvalues of L the most dominant oscillation has period $T = 23.92$ months. The Welch's periodograms of the data and four of the LIMs have their maximum at $T = 23.81$ months. The remaining LIM shows a period of 24.09 as the most dominant oscillation. This indicates that the LIM is capable of reproducing the dominant frequencies and that the two methods of finding them lead to very similar results. Therefore, the feedback matrices of LIMs can be used to identify the most dominant frequency and its e-folding time in an oscillating time series.

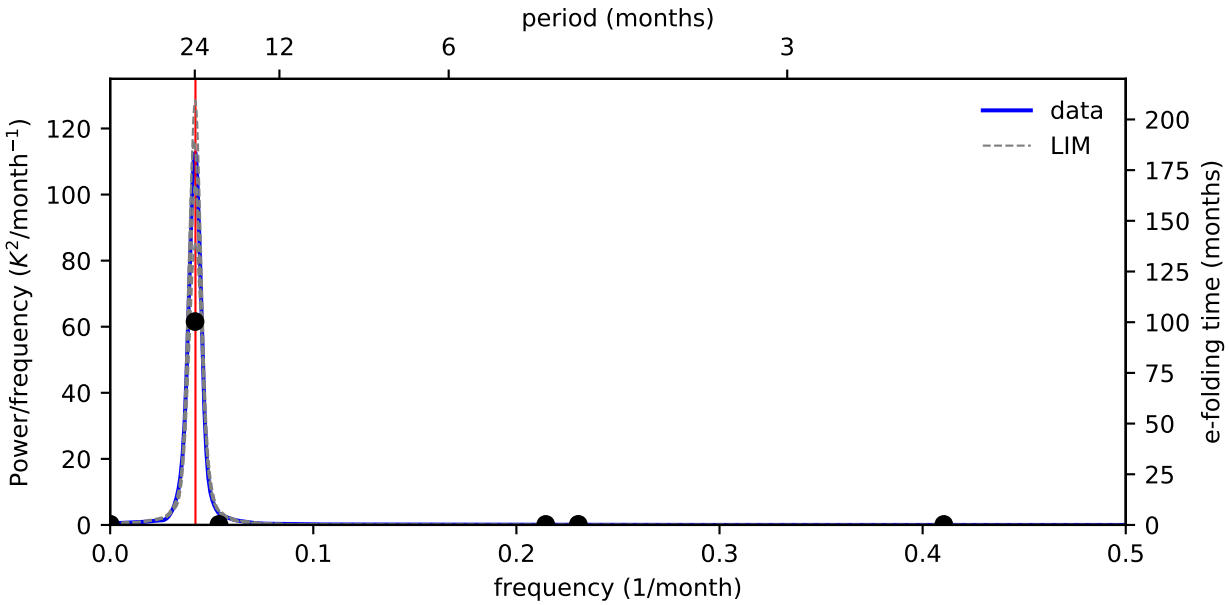

Figure 6: Black dots: Inverse of the real part of the eigenvalues of L (e-folding time) plotted against the imaginary part (frequency)(right y-axis). Blue (grey dashed) lines: Welch's periodograms of the data (LIM) (left y-axis).

4 Results and Discussion

4.1 Simple Approaches

The analysis of the moving average (MA) (of both, the CMIP6- and MPI-ensemble) revealed the results presented in table 2. The MA of the first three PCs of the CMIP6-ensemble can be seen in figure 7. The slope of the regression line of the PC-Index (PC1) is only $5 \cdot 10^{-6}$ K/month. The slopes of the second and third PC are similarly small. This indicates that there is no noticeable trend in the PC-Index or secondary patterns. Thus, the index is not (strongly) shifted to more positive than negative values with a warming climate.

Table 2: Slopes of regression lines of ensemble means for moving average and standard deviation for CMIP6- and MPI-ensemble. Also see figures 7, 8,9 and 10.

	CMIP6-ensemble		MPI-ensemble	
	Slope Moving average (K/month)	Slope Standard Deviation (K/month)	Slope Moving Average (K/month)	Slope Standard Deviation (K/month)
PC1	$5.0 \cdot 10^{-6}$	$3.83 \cdot 10^{-5}$	$-1.1 \cdot 10^{-6}$	$-5.01 \cdot 10^{-5}$
PC2	$6.2 \cdot 10^{-6}$	$3.01 \cdot 10^{-5}$	$-1.03 \cdot 10^{-5}$	$-3.76 \cdot 10^{-5}$
PC3	$3.6 \cdot 10^{-6}$	$2.66 \cdot 10^{-5}$	$5.9 \cdot 10^{-6}$	$-4.15 \cdot 10^{-5}$

As mentioned in section 3.1, a trend towards stronger EN *and* stronger LN or an increase or decrease in both their frequencies would not show in the moving average but rather in a larger or smaller standard deviation. The standard deviation over 30-year moving windows for the first 3 PCs of the CMIP6-ensemble can bee seen in figure 8 and the values of the slopes of the regression line are also denoted in table 2. With a value of $3.83 \cdot 10^{-5}$ K/month, the slope of the regression line for the PC-Index (PC1) is similarly small for the standard deviation as it is for the MA, which indicates no pronounced trend in the standard deviations either. This test therefore provides no indication that EN- and LN-events do both become noticeably stronger or more frequent.

The fit of the regression line does not only deliver the estimated parameters themselves but also their standard deviation. In this case, the standard deviations are much smaller than the estimated parameters themselves, so that the slope plus or minus its standard deviation still has the same sign. Therefore, I can be confident that the calculated trends are truly positive (negative), even though very small.

With these two simple tests I therefore come to the conclusion that the trends in the CMIP6-ensemble are, even though definitely positive, extremely small if not negligible. The same analysis can be done for the MPI-ensemble (see table 2 and figures 9 and 10). In this case the trends are negative, indicating a shift towards more negative values in the PC-Index (PC1) and a reduction in amplitude or frequency of both EN- and LN-events. However, the trends for the MPI-ensemble are also extremely small.

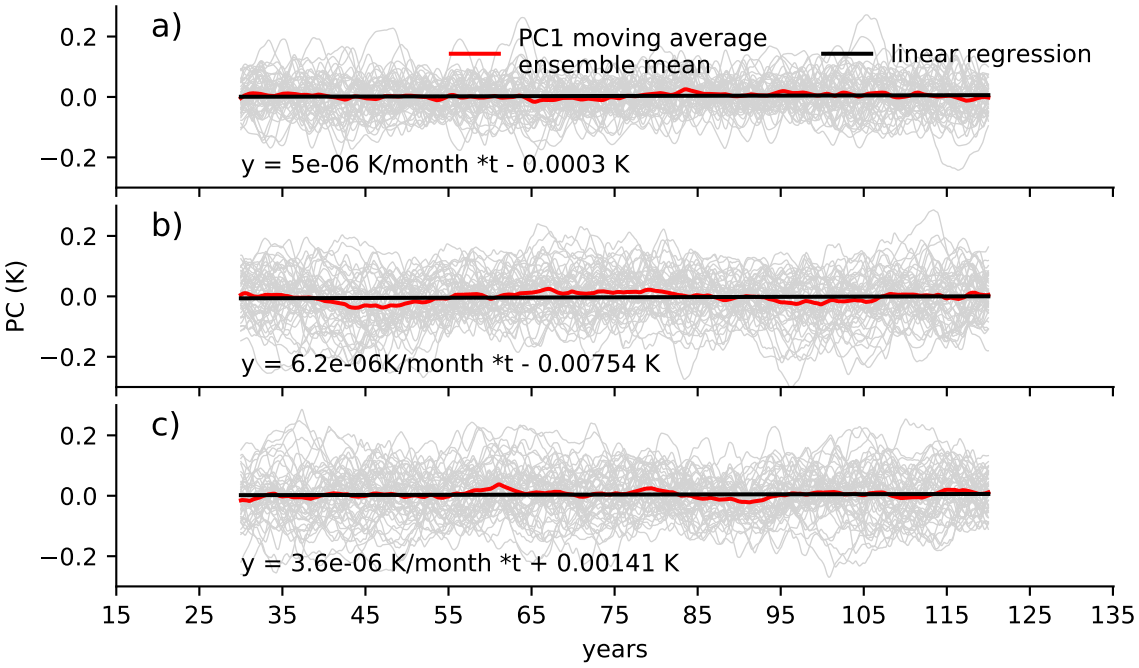

Figure 7: CMIP6-ensemble. Moving average of the PC-Index (a), the second (b) and third PC (c) for each model (grey). The ensemble mean is shown in red, a regression line has been fitted to the ensemble mean (black).

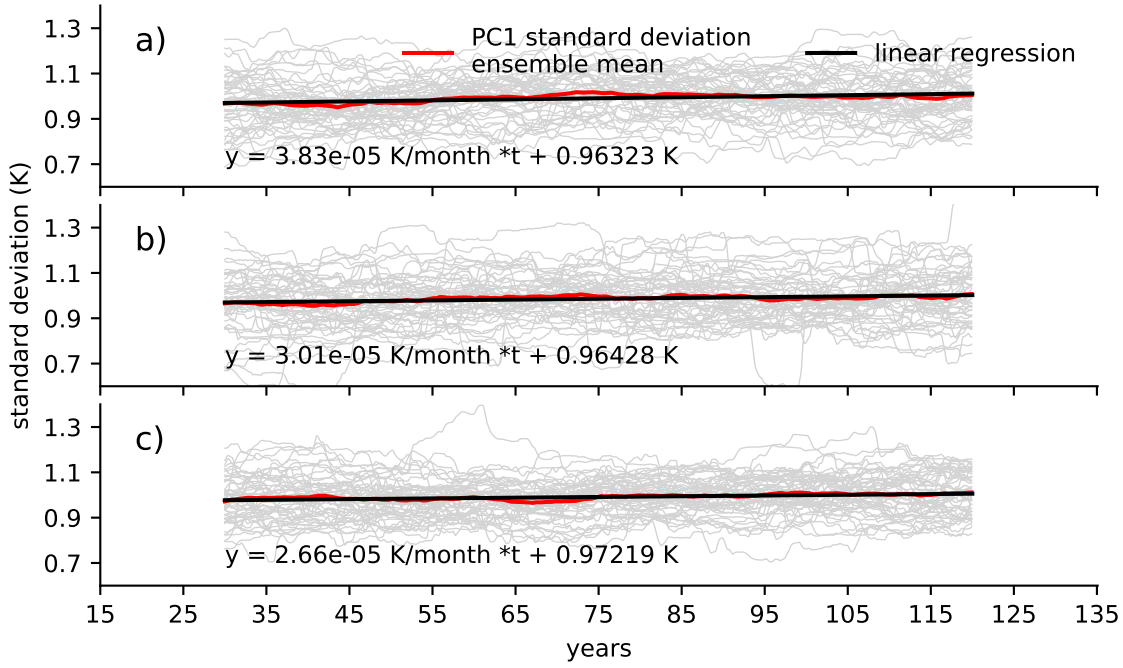

Figure 8: CMIP6-ensemble. Standard deviation of the PC-Index (a), the second (b) and third PC (c) over a 30-year moving window for each model (grey). The ensemble mean is shown in red, a regression line has been fitted to the ensemble mean (black).

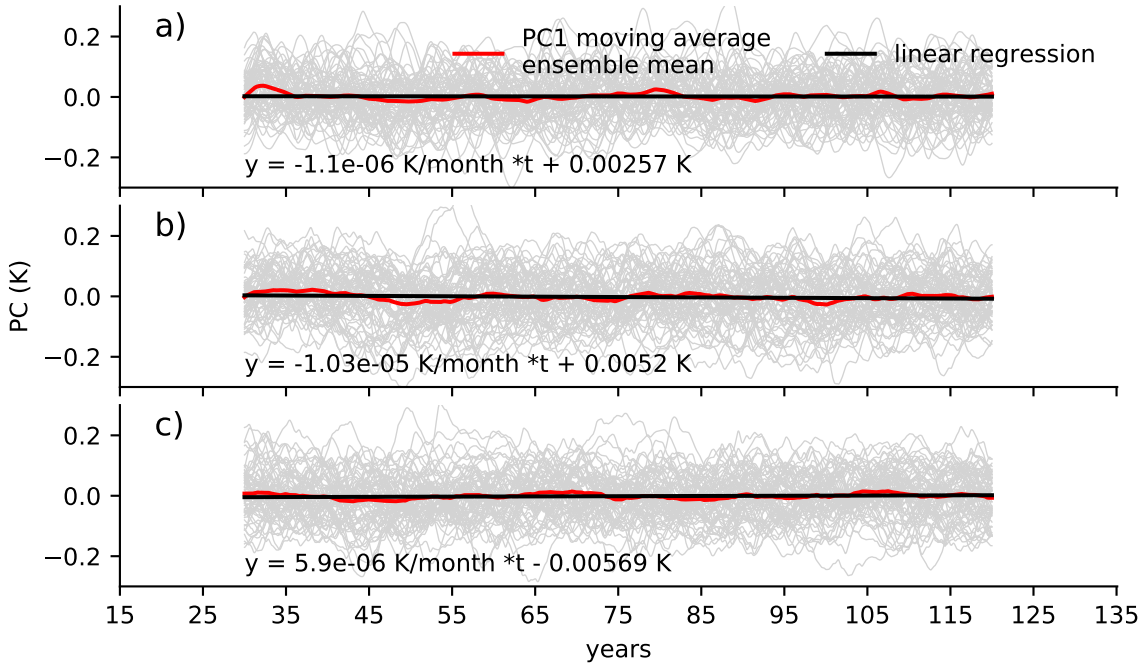

Figure 9: MPI-ensemble. Moving average of the PC-Index (a), the second (b) and third PC (c) for each model (grey). The ensemble mean is shown in red, a regression line has been fitted to the ensemble mean (black).

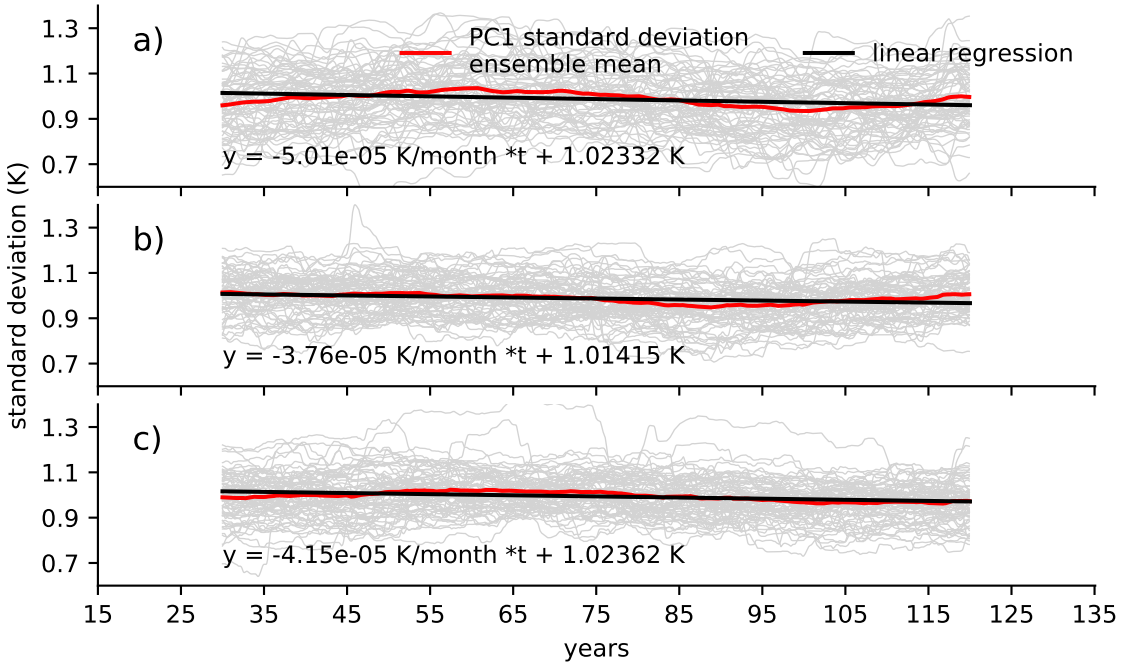

Figure 10: MPI-ensemble. Standard deviation of the PC-Index (a), the second (b) and third PC (c) over a 30-year moving window for each model (grey). The ensemble mean is shown in red, a regression line has been fitted to the ensemble mean (black).

As mentioned in section 3.1, there are studies (e.g. Cai et al. 2014 and 2015b) that suggest a relevant change in ENSO frequency. In order to test if the ENSO frequency changes in the two ensembles I analyse here, I counted EN- and LN-like conditions as well as events. The results of this analysis are summarised in table 3. The condition is considered EN- (LN-) like, when the PC-Index exceeds a threshold of 0.5°C (−0.5°C). It is called a EN (LN) event whenever this condition is met for at least 5 consecutive months (NOAA CPC , 2020b).

Table 3: Slopes of regression lines of ensemble means for EN/LN occurences for CMIP6- and MPI-ensemble. Also see figures 11 and 12.

	CMIP6-ensemble	MPI-ensemble
slope EN-like conditions (month^{-1})	$1.72 \cdot 10^{-3}$	$-1.41 \cdot 10^{-3}$
slope LN-like conditions (month^{-1})	$1.72 \cdot 10^{-3}$	$-2.67 \cdot 10^{-3}$
slope EN events (month^{-1})	$4.3 \cdot 10^{-4}$	$5.8 \cdot 10^{-4}$
slope LN events (month^{-1})	$2.8 \cdot 10^{-4}$	$1.7 \cdot 10^{-4}$

For the CMIP6-ensemble, the number of occurrences can be seen in figure 11. Again, the slopes of the regression lines are very small, which indicates no pronounced trend in periodicity either. For the whole time period an average of just above 8 ENs and LNs per 30-year window is detected, which corresponds to one ENSO cycle every 3 to 4 years on average. For the MPI-ensemble the results are very similar, only the average number of EN and LN events is smaller with an average between 5 and 6 and corresponds to the longer period of 5 to 6 years (Fig. 12). For both ensembles these periods lie within the ENSO-band of 3 to 7 years.

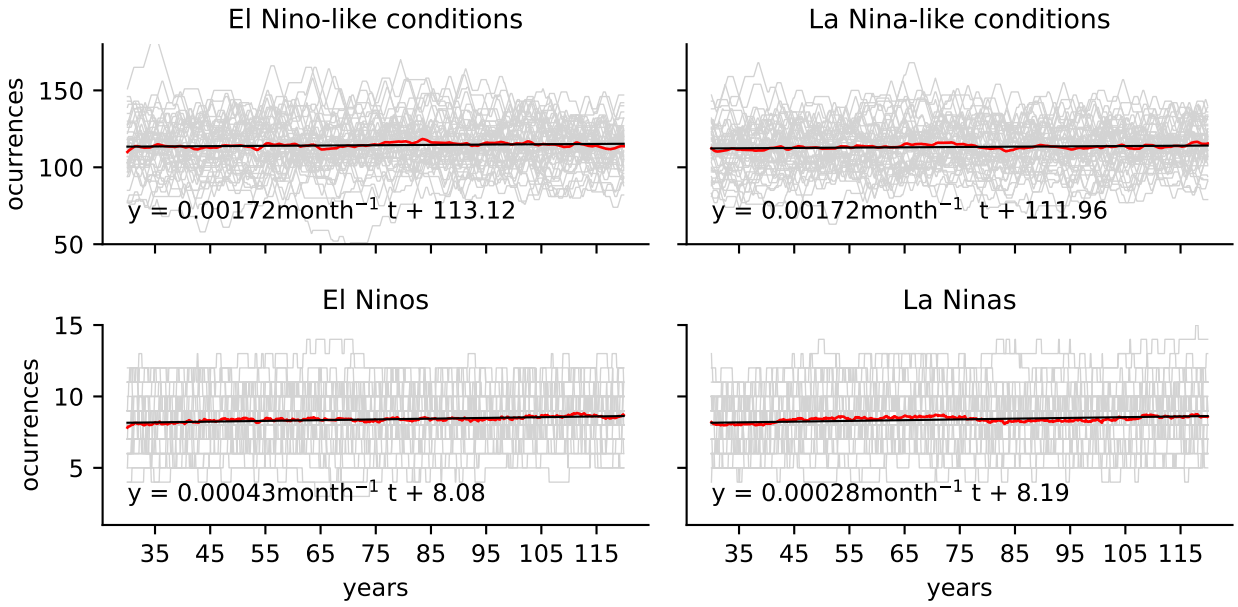

Figure 11: CMIP6-ensemble. Occurrences EN-/ LN-Conditions (upper panels) and events (lower panels) for every model (grey). The ensemble mean is denoted in red and the regression line in black.

In previous studies (Guilyardi et al., 2009; Berner et al., 2020; Cai et al., 2015a) it has become apparent that there is not much consistency between the predictions of ENSO future in the different models participating in CMIP. If the different models in the CMIP6-ensemble come

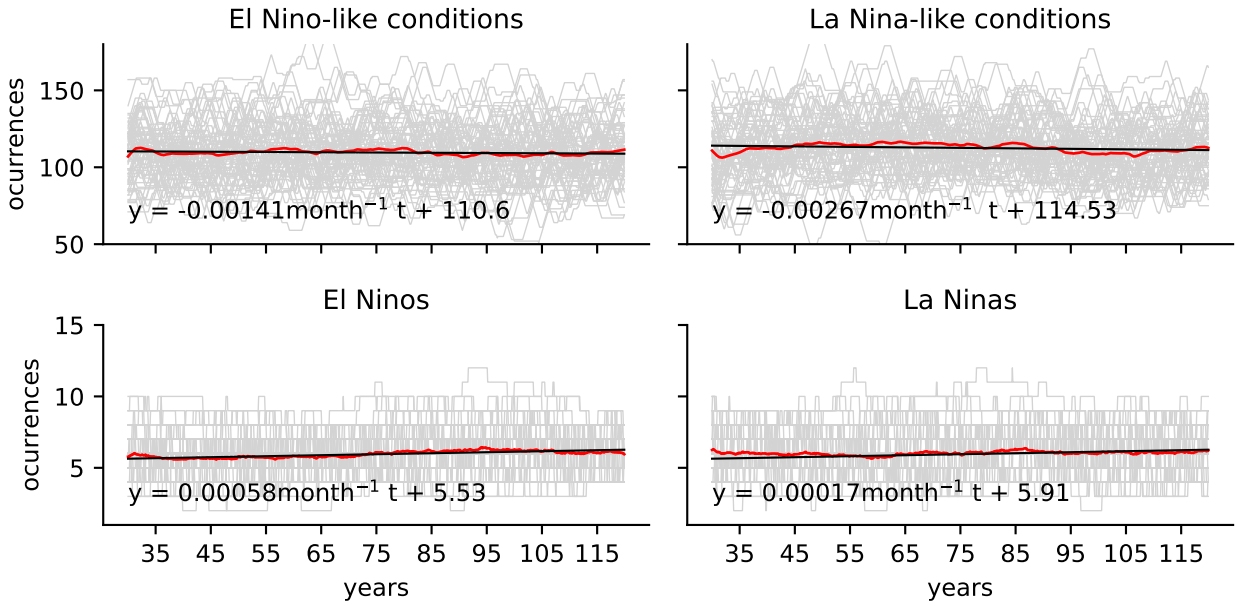

Figure 12: MPI-ensemble. Occurrences EN-/ LN-Conditions (upper panels) and events (lower panels) for every model (grey). The ensemble mean is denoted in red and the regression line in black.

to contradicting conclusions too, the analysis of the ensemble mean might not be conclusive at all, and further analysis of the single members is necessary. Therefore, the values of the trends in each model are depicted in figure 13. It is obvious that the different models do indeed predict different outcomes for ENSO periodicity. The errors of the estimated gradients are considerably smaller than their value, so however small the gradient is, its sign does not change within the range of uncertainty. Again, the trends are very small if not negligible. Figure 14 shows the same results as figure 13 but for the MPI-ensemble. It becomes clear that the variability within the MPI-ensemble is similarly large as in the CMIP6-ensemble. This means that internal climate variability (which can be estimated from the MPI-ensemble) is as large as the variability due to differences between the models of the CMIP6-ensemble. Reality could evolve like any of the ensemble members and they can be quite different from the ensemble mean. This means that there remains an irreducible uncertainty when predicting ENSO on a time scale of 150 years because of the internal climate variability.

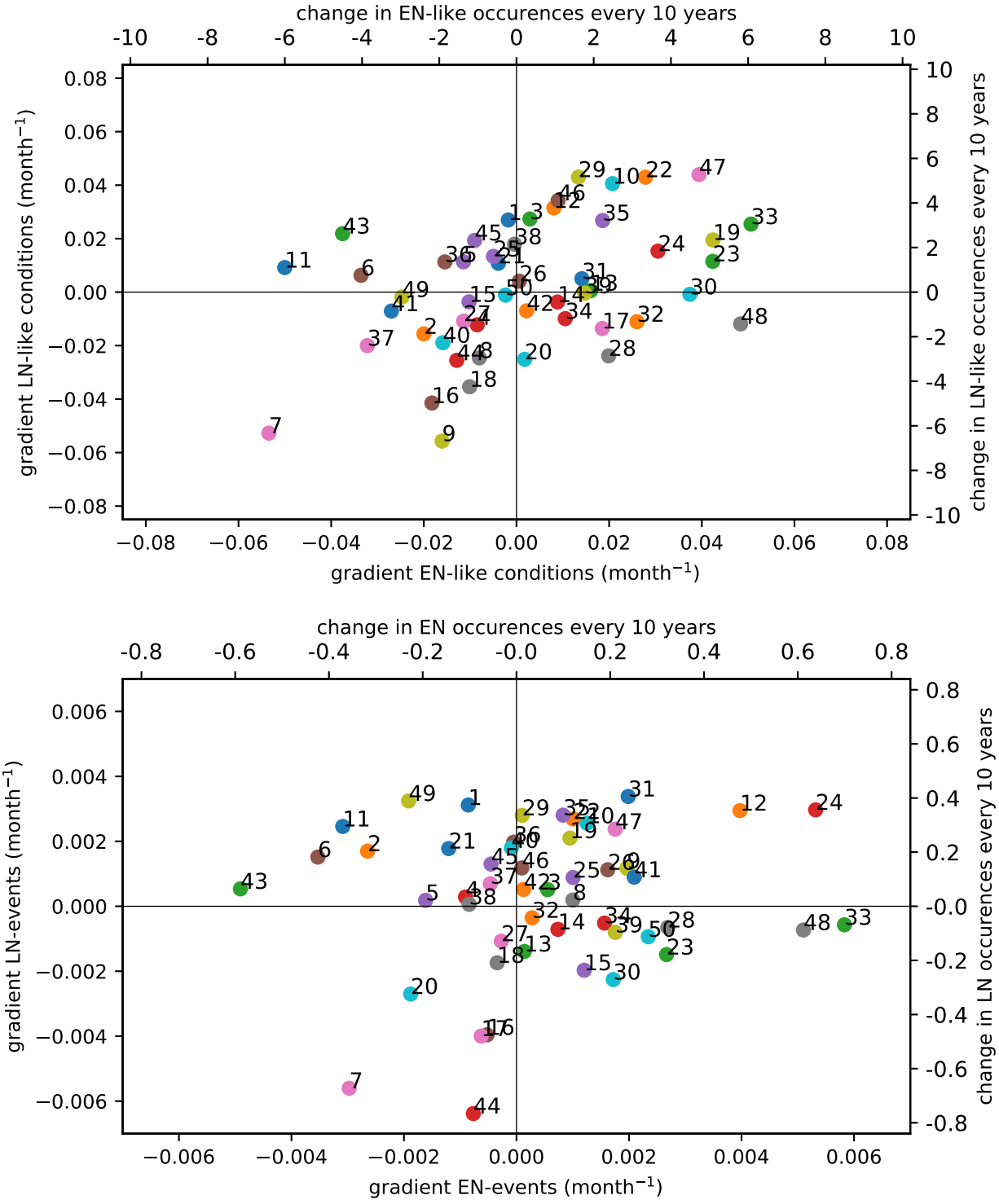

Figure 13: CMIP6-ensemble. Gradients of the trends in EN/LN-like conditions (top) and EN/LN events (bottom) for each model. Values towards the top of the plot indicate increasing number of LN conditions/events, values toward the right of the plot indicate an increasing number of EN conditions/events. Numbers correspond to models as in table 1.

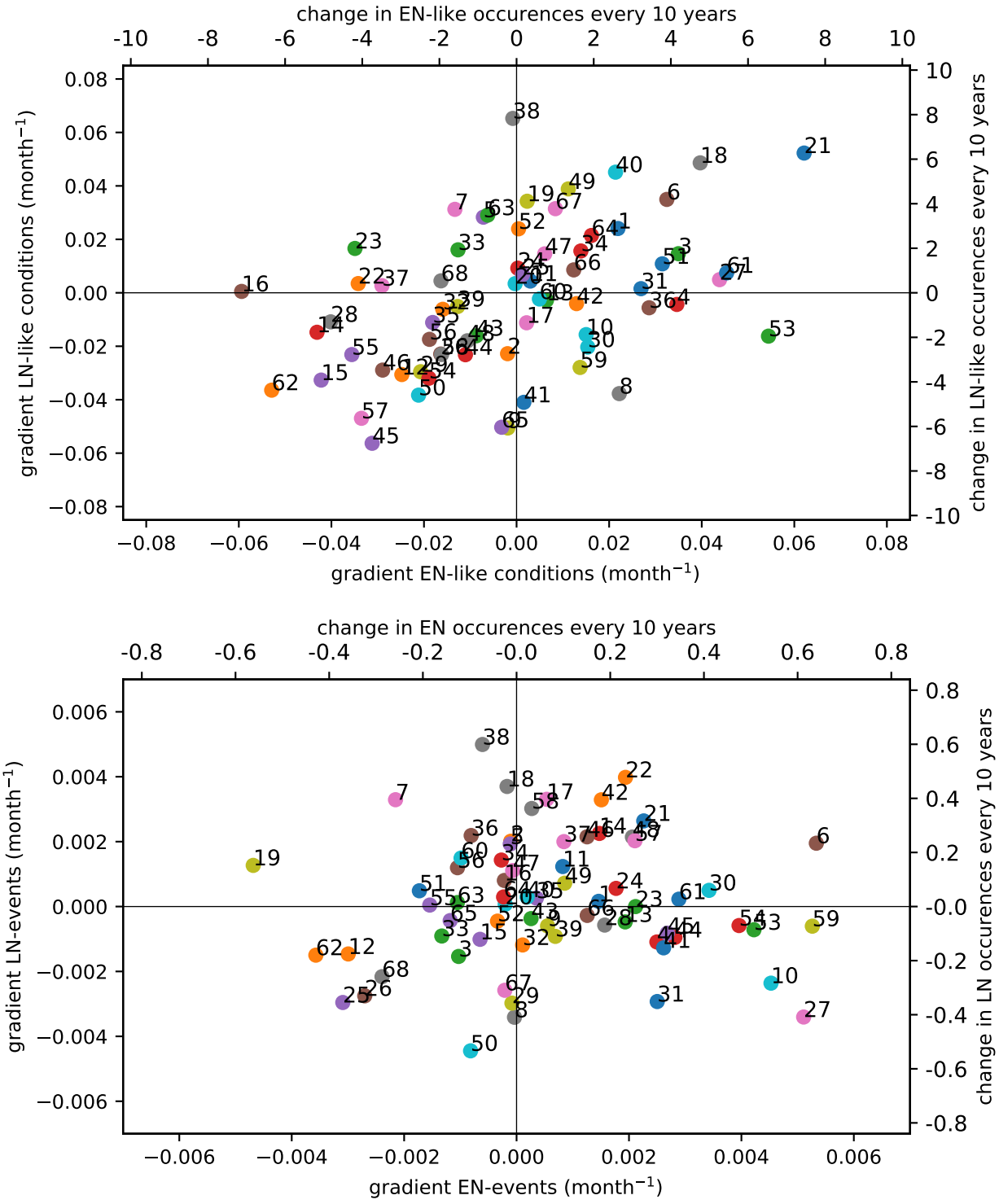

Figure 14: Same as figure 13 but for MPI-ensemble.

4.2 Linear Inverse Model

Since the simple methods described above failed to pick up pronounced changes in ENSO behaviour, the purpose of the following analysis is to test whether more sophisticated methods are better suited for the task. In particular, the hypothesis shall be tested as to whether Linear Inverse Models (LIMs) are able to find changes in ENSO periodicity, since, as described in section 3.3 the feedback matrix is a measure that describes the oscillatory behaviour in a relatively detailed way. For this purpose, I fitted LIMs to the whole 120-year time series as well as to three consecutive 40-year periods (P1-P3). By fitting to the whole ensemble as well as to single members, it should be tested whether LIMs fitted to single ensemble members are representative for the ensemble and can therefore be used to achieve robust results.

I fitted a LIM to the complete MPI-ensemble by calculating the EOF for the stacked data and averaging the covariance matrices (see section 3.2). The Welch's periodograms of the ensemble, the LIMs, and their mean can be seen in figure 15. It is clear that the mean of the periodograms of the ensemble data (solid lines) and the mean of the periodograms of the LIM fits (thick dashed lines) are very similar for all three periods. But it also becomes apparent that the single realisations of the LIM have an even greater spread than the single ensemble members. This means that, in order to get a reliable result from Welch's periodograms of LIM fits, an ensemble of LIM realisations is needed.

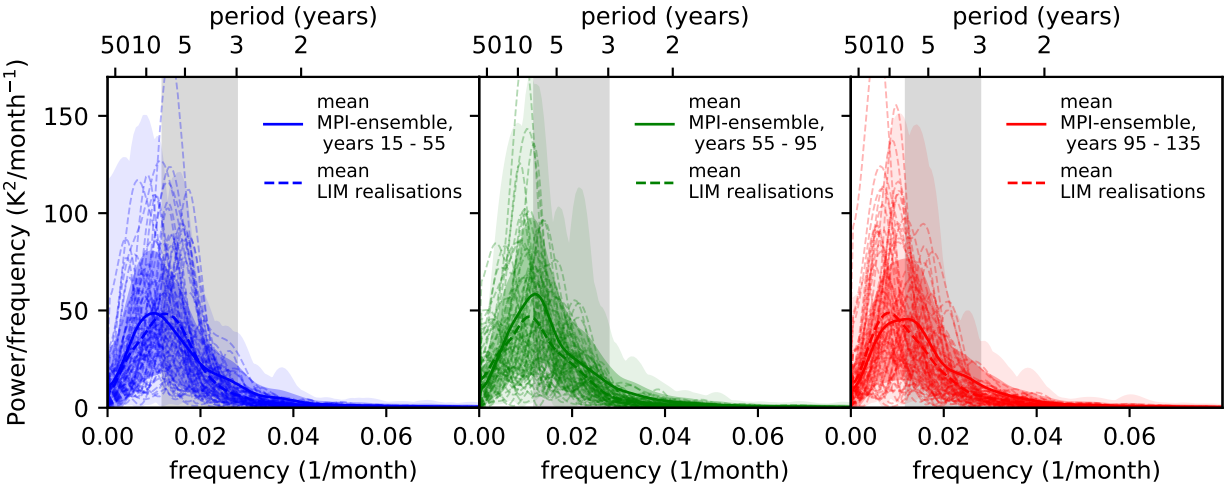

Figure 15: Power spectral density (PSD) of PC-Index as a function of frequency for the first (left), second (middle), and last (right) 40 years of the time series. Coloured solid lines denote the mean of the MPI-ensemble spectra, light shading denotes the extremes, and dark shading the standard deviation of the ensemble member spectra, respectively. Thin dashed lines denote the PSDs of the different realisations of the LIM fitted to the whole ensemble, the thick dashed line denotes their mean. Grey shading denotes the ENSO-band between 3 and 7 years.

As discussed in section 3.3, the dominant frequencies of an oscillator modelled with a LIM can be determined by analysing a periodogram of the data or the eigenvalues of the feedback matrix of the LIM. In this case it can be expected that the peak of the periodogram lies in the ENSO-band and that there is one frequency with a much longer e-folding time than all others, which also lies in the ENSO-band. In Figure 16, both approaches are displayed for the whole time series as well for the three sub-periods. It becomes apparent that, corresponding

to the peaks in the periodograms, there is one frequency with a long e-folding time in the same frequency range. The periodograms and the eigenvalues do not show exactly the same frequency. This is because the periodogram shows a mixture of all frequencies, which results in a shift in frequencies due to secondary oscillations. Figure 16 shows that the dominant frequencies seem to become smaller for the later periods and the e-folding times shorter (the green and red dots are further left and lower). This indicates that in a warmer climate ENSO cycles become longer and the time of decay shorter. A similar result was found by Park et al. (2009) who analysed an ensemble of eight model simulations for a similar experiment.

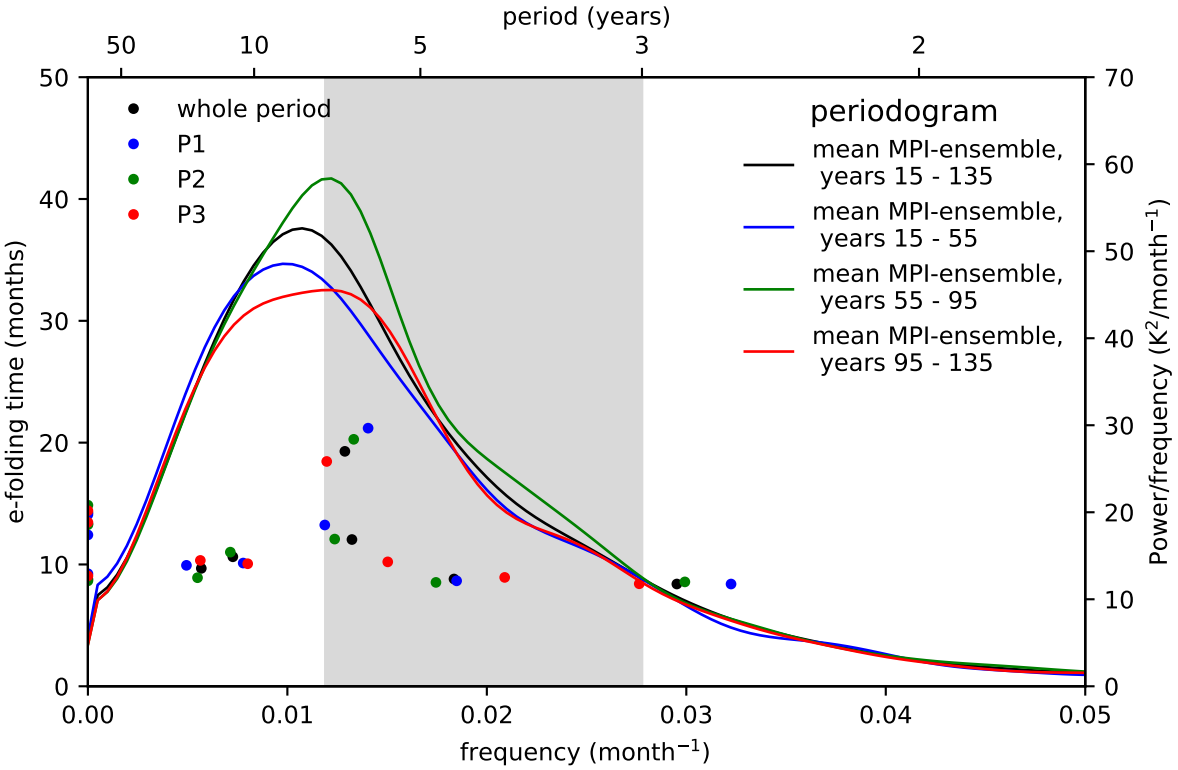

Figure 16: MPI-ensemble. Welch's periodograms (ensemble mean, lines, right y-axis) of the data for the whole time series (black), the first (blue), second (green) and last (red) 40 years of the time series. E-folding time plotted against frequency, derived from feedback matrices L for each period (dots, left y-axis).

It is important to investigate whether this trend is really statistically significant or a mere coincidence. I checked for this by selecting four different sub-samples of half the ensemble size (the first and second half, as well as the even and odd members). The analysis for these sub-samples yield overall the same results for the shift in period (figures corresponding to Fig. 16 can be found in the appendix). This indicates that there actually is a statistically significant development, but this still needs to be confirmed by more thorough analyses. The shift in the e-folding time is not consistent in the four sub-samples. This quick method can therefore not confirm a trend and further analysis is necessary.

Now the question of interest is whether the same conclusions can be drawn when fitting LIMs to single members of the ensemble. To answer that question, the e-folding time and frequencies are derived for each ensemble member. This is done by fitting a LIM to each member as described in section 3.2 (for 68 resulting plots, see appendix). In figure 17, all the resulting e-folding times are plotted in one panel per period for better visualisation. Qualitatively, the

spread between the results of the different fits is by far greater than the difference between the periods in the fit to the complete ensemble. An additional illustration is provided in figure 18. Here, the medians and interquartile ranges of the light dots from figure 17, as well as their means are displayed. It can be seen that the averaged results lie in the same range as the ensemble fit, but they do not exhibit the same trend. From these results it seems likely that there is no trend and the differences origin from internal variability. The dominant frequencies and their change that are determined from the LIMs fitted to single ensemble members are therefore not representative for the frequencies and changes determined from the LIM fitted to the whole ensemble. Whether there is actually a trend, as suggested by the latter, has to be investigated further, for example by using the bootstrapping method.

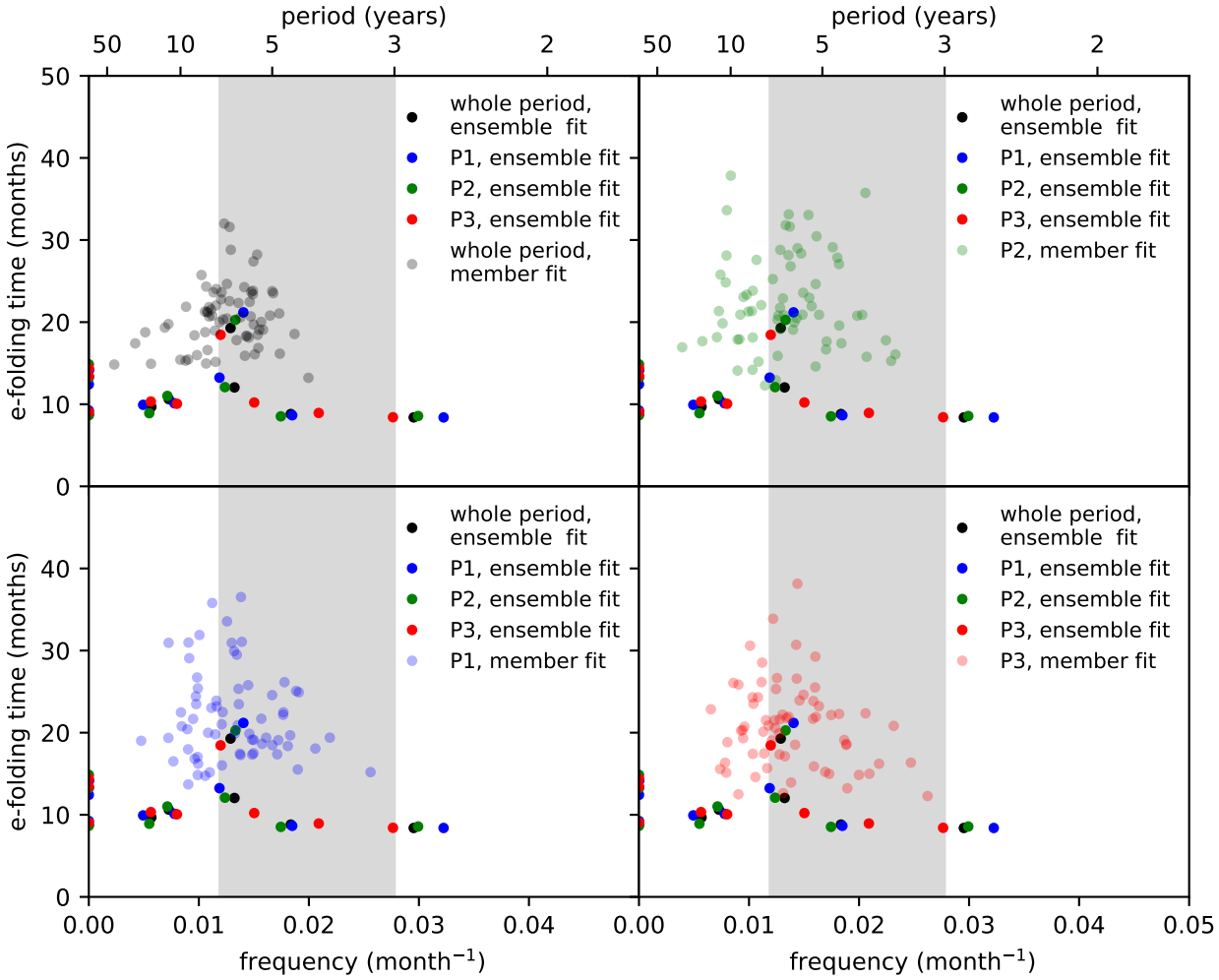

Figure 17: MPI-ensemble. E-folding time (inverse of the real part of the eigenvalues of L) plotted against the frequency (imaginary part) for the whole period (black), the first (blue), second (green) and third (red) 40 years of the time series. Solid dots represent the fits to the whole ensemble, while light dots represent the fits to the different single members. For better visibility of the latter, they have been plotted in separate panels.

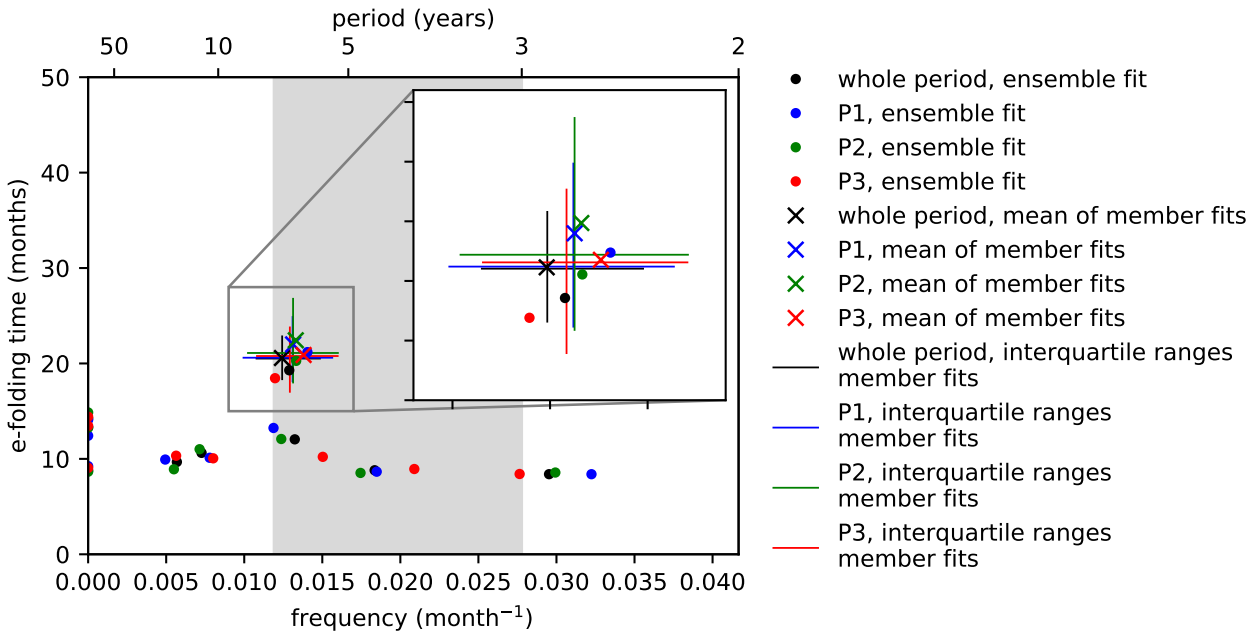

Figure 18: MPI-ensemble. E-folding time (inverse of the real part of the eigenvalues of L, derived from the fit to the whole ensemble) plotted against the frequency (imaginary part) for the whole period (black dots), the first (blue dots), second (green dots) and third (red dots) 40 years of the time series. Crosses denote the means of the most dominant frequencies, calculated from the fits to single ensemble members. Lines mark their interquartile ranges.

5 Summary and Outlook

El Niño Southern Oscillation (ENSO) has far reaching consequences in many parts of the world. Understanding and predicting it is therefore a major focus in current climate research. In particular, the question on how ENSO will react to a changing climate is of great interest. I addressed this question with different methods, using two General Circulation Model (GCM) ensembles. One of the ensembles is a multi-model ensemble of models participating in the 1 percent CO_2 (1pctCO2) experiment of CMIP6 (CMIP6-ensemble). The other is an initial conditions ensemble of the MPI-ESM-LR model, run for the same experiment in CMIP5 (MPI-ensemble). The ENSO-Index used in this work is based on the principle component (PC) of the first empirical orthogonal function (EOF) of the sea surface temperature (SST) data. This index only requires one variable and describes the same variations as the commonly used Ocean Niño Index (ONI). Together with the higher PCs it describes the SST oscillations even more completely. A Linear Inverse Model (LIM) can be fitted to the first 15 PCs of the SST, which can then be used for further analysis.

The analysis of the moving average (MA) of said PC-Index showed that in the CMIP6-ensemble there is an almost unnoticeable trend towards more positive PC-Index values, whereas it is similarly small but negative for the MPI-ensemble. Additionally, the standard deviation was analysed over a moving 30-year window. As a result an extremely small increase of the standard deviation for the CMIP6-ensemble and a decrease for the MPI-ensemble was found. The trends are so small, however, that I can not conclude from this analysis whether there is going to be a detectable change in ENSO-behaviour.

Previous work has shown that there might be a considerable change in ENSO-frequency (Cai et al., 2015b, 2014). By counting ENSO-like conditions and -events I wanted to verify this conclusion. Again, I could only find extremely small trends in both ensembles, so that I can not confirm that there will be pronounced changes to ENSO-frequency in the analysed 120 years.

Because changes were expected to be quite subtle, I explored the possibility of using LIM simulations to find changes, in addition to the simple approaches named above. For this purpose I investigated if LIM fitting is suitable for detecting changes in ENSO-frequency. By fitting LIMs to the complete MPI-ensemble as well as to each of the 68 members, I could test if LIMs fitted to single realisations of one climate model represent the properties of the entire ensemble accurately. I found that this is not the case. The LIMs fitted to single members differ substantially and are not representative for the entire ensemble. Therefore one can not fit LIMs to the members of a multi-model ensemble (like the CMIP6-ensemble) to simply compare their predictions on ENSO's future behaviour.

But even if the LIMs fitted to the single members are not useful for further analysis, the fit to the complete MPI-ensemble delivered promising results. The eigenvalues of the feedback matrix of the LIM contain information about the existing frequencies and their e-folding times. This (as well as the analysis of the Welch's periodogram of the data) yielded a very dominant frequency within the ENSO-band.

In order to identify changes over the analysed 120-years of the simulation period, I split the time series in three consecutive 40-year sub-series. When comparing the results from LIMs fitted to these three sub-series, it became apparent that the dominant frequency becomes smaller.

This indicates that, with a warming climate, ENSO cycles are predicted to become longer and El Niño (EN)- and La Niña (LN)-events therefore less frequent. The simulation of the MPI-ensemble predicts an increase of the ENSO-period from 5.93 to 7.02 years (blue and red dots in Fig. 16). This means that the number of ENSO cycles happening within a 40-year period is projected to decrease by about one event (from about 6.8 to just 5.7). When comparing this to the lower panel of figure 14 another finding becomes apparent. The most extreme members in this figure predict an increase or decrease of EN- and/or LN-events by up to 0.6 per decade. This means that during the simulated period of 120 years the number of EN-/LN-events will increase (or decrease) by over 7. This is obviously a greater change than the analysis of the LIMs of the three sub-period showed. It becomes clear that the range of possible ENSO changes is more relevant than the change that can be determined by analysing the complete ensemble. Reality is most likely not going to develop like the ensemble mean but like one of the members. Therefore the great spread between the possible outcomes presents a challenge, especially when thinking about adaptation or mitigation measures that are supposed to protect society and the environment from the extreme weather events caused by EN- and LN-events.

As mentioned in chapter 4, further investigations need to be carried out in order to establish if the trend towards longer ENSO periods is actually statistically significant. This, however, went beyond the scope of this work but is recommended to be done in due course by e.g. using the bootstrapping method. The bootstrapping method is a statistical method to estimate the accuracy of properties estimated from (small) samples (Boos, 2003; Efron and Tibshirani, 1994). By resampling (with replacement) the number of samples is increased, which can then be used to determine these properties.

In this work the difference between LIMs fitted to single ensemble members and LIMs fitted to a whole ensemble has only been examined using the MPI-ensemble. It might be of interest to do this for the CMIP6-ensemble as well. In order to do this, the outputs of all members have to be regridded to a common grid, such that a common EOF can be calculated.

Another topic that follow-up research could address is a multi-model ensemble contributing to CMIP5. Since the analysis of the MPI-ensemble (which dates from CMIP5) showed a slight decrease in the PC-index, it's standard deviation and the ENSO frequency, it would be interesting to see if a multi-model ensemble of the CMIP5 generation shows the same features.

Finally, to gain better insight into the likely ENSO changes it would be very interesting to perform the analysis that was done here with the MPI-ensemble with initial conditions ensembles of the models contributing to CMIP6.

References

Berner, Judith, Christensen, Hannah M., and Sardeshmukh, Prashant D. Does ENSO Regularity Increase in a Warming Climate? *Journal of Climate*, 33(4):1247–1259, 2020. ISSN 0894-8755. doi: 10.1175/JCLI-D-19-0545.1. URL https://doi.org/10.1175/JCLI-D-19-0545.1.

Boos, Dennis D. Introduction to the bootstrap world. *Statist. Sci.*, 18(2):168–174, 2003. doi: 10.1214/ss/1063994971. URL https://doi.org/10.1214/ss/1063994971.

Cai, Wenju, Borlace, Simon, Lengaigne, Matthieu, van Rensch, Peter, Collins, Matt, Vecchi, Gabriel, Timmermann, Axel, Santoso, Agus, McPhaden, Micheal J., Wu, Lixin, England, Matthew H., Wang, Guojian, Guilyardi, Eric, and Jin, Fei-Fei. Increasing frequency of extreme El Niño events due to greenhouse warming. *Nature Climate Change*, 4:111–116, 2014. doi: 10.1038/nclimate2100. URL https://doi.org/10.1038/nclimate2100.

Cai, Wenju, Santoso, Angus, Wang, Guojian, Yeh, Sang-Wook, An, Soon-Il, Cobb, Kim M., Collins, Matt, Guilyardi, Eric, , Jin, Fei-Fei, Kug, Jong-Seong, Lengaigne, Matthieu, McPhaden, Micheal J., Takahashi, Ken, Timmermann, Axel, Vecchi, Gabriel, Watanabe, Masahiro, and Wu, Lixin. ENSO and greenhouse warming. *Nature Climate Change*, 5:849–859, 2015a. doi: 10.1038/nclimate2743. URL https://doi.org/10.1038/nclimate2743.

Cai, Wenju, Wang, Guojian, Santoso, Agus, McPhaden, Michael J., Wu, Lixin, Jin, Fei-Fei, Timmermann, Axel, Collins, Mat, Vecchi, Gabriel, Lengaigne, Matthieu, England, Matthew H., Dommenget, Dietmar, Takahashi, Ken, and Guilyardi, Eric. Increased frequency of extreme La Niña events under greenhouse warming. *Nature Climate Change*, 5:132–137, 2015b. doi: 10.1038/nclimate2492. URL https://doi.org/10.1038/nclimate2492.

Capotondi, Antonietta and Sardeshmukh, Prashant D. Is El Niño really changing? *Geophysical Research Letters*, 44(16):8548–8556, 2017. doi: 10.1002/2017GL074515. URL https://agupubs.onlinelibrary.wiley.com/doi/abs/10.1002/2017GL074515.

Dawson, Andrew. eofs: A Library for EOF Analysis of Meteorological, Oceanographic and Climate Data. *Journal of Open Research Software*, 4(1):e14, 2016. doi: 10.5334/jors.122. URL http://doi.org/10.5334/jors.122.

Deser, C., Lehner, F., Rodgers, K. B., Ault, T., Delworth, T. L., DiNezio, P. N., Fiore, A., Frankignoul, C., Fyfe, J. C., Horton, D. E., Kay, J. E., Knutti, R., Lovenduski, N. S., Marotzke, J., McKinnon, K. A., Minobe, S., Randerson, J., Screen, J. A., Simpson, I. R., and Ting, M. Insights from Earth system model initial-condition large ensembles and future prospects. *Nature Climate Change*, 10:277–286, 2020. URL https://doi.org/10.1038/s41558-020-0731-2.

Dommenget, Dietmar, Bayr, Tobias, and Frauen, Claudia. Analysis of the non-linearity in the pattern and time evolution of El Niño southern oscillation. *Climate Dynamics*, 40:2825–2847, 2013. doi: 10.1007/s00382-012-1475-0. URL https://doi.org/10.1007/s00382-012-1475-0.

Efron, B. and Tibshirani, R.J. *An Introduction to the Bootstrap*. Chapman & Hall/CRC Monographs on Statistics & Applied Probability. Taylor & Francis, 1994. ISBN 9780412042317. URL https://books.google.de/books?id=gLlpIUxRntoC.

Giorgetta, Marco A., Jungclaus, Johann, Reick, Christian H., Legutke, Stephanie, Bader, Jürgen, Böttinger, Michael, Brovkin, Victor, Crueger, Traute, Esch, Monika, Fieg, Kerstin, Glushak, Ksenia, Gayler, Veronika, Haak, Helmuth, Hollweg, Heinz-Dieter, Ilyina, Tatiana, Kinne, Stefan, Kornblueh, Luis, Matei, Daniela, Mauritsen, Thorsten, Mikolajewicz, Uwe, Mueller, Wolfgang, Notz, Dirk, Pithan, Felix, Raddatz, Thomas, Rast, Sebastian, Redler, Rene, Roeckner, Erich, Schmidt, Hauke, Schnur, Reiner, Segschneider, Joachim, Six, Katharina D., Stockhause, Martina, Timmreck, Claudia, Wegner, Jörg, Widmann, Heinrich, Wieners, Karl-H., Claussen, Martin, Marotzke, Jochem, and Stevens, Bjorn. Climate and carbon cycle changes from 1850 to 2100 in MPI-ESM simulations for the Coupled Model Intercomparison Project phase 5. *Journal of Advances in Modeling Earth Systems*, 5(3): 572–597, 2013. doi: 10.1002/jame.20038. URL https://agupubs.onlinelibrary.wiley.com/doi/abs/10.1002/jame.20038.

Guilyardi, Eric, Wittenberg, Andrew, Fedorov, Alexey, Collins, Mat, Wang, Chunzai, Capotondi, Antonietta, van Oldenborgh, Geert Jan, and Stockdale, Tim. Understanding El Niño in Ocean–Atmosphere General Circulation Models: Progress and Challenges. *Bulletin of the American Meteorological Society*, 90(3):325–340, 03 2009. ISSN 0003-0007. doi: 10.1175/2008BAMS2387.1. URL https://doi.org/10.1175/2008BAMS2387.1.

Kestin, Tahl S., Karoly, David J., Yano, Jun-Ichi, and Rayner, Nicola A. Time–Frequency Variability of ENSO and Stochastic Simulations. *Journal of Climate*, 11(9):2258–2272, 1998. ISSN 0894-8755. doi: 10.1175/1520-0442(1998)011⟨2258:TFVOEA⟩2.0.CO;2. URL https://doi.org/10.1175/1520-0442(1998)011<2258:TFVOEA>2.0.CO;2.

Kim, Seon Tae, Cai, Wenju, Jin, Fei-Fei, Santoso, Agus, Wu, Lixin, Guilyardi, Eric, and An, Soon-Il. Response of El Niño sea surface temperature variability to greenhouse warming. *Nature Climate Change*, 4:786–790, 2014. doi: 10.1038/nclimate2326. URL https://doi.org/10.1038/nclimate2326.

Kraus, Helmut. *Die Atmosphäre - Eine Einführung in die Meteorologie*. Springer-Verlag, 3 edition, 2004. ISBN:3-540-20656-6.

Lin, Renping, Zheng, Fei, and Dong, Xiao. ENSO Frequency Asymmetry and the Pacific Decadal Oscillation in Observations and 19 CMIP5 Models. *Advances in Atmospheric Sciences*, 35:495–506, 2018. doi: 10.1007/s00376-017-7133-z. URL https://doi.org/10.1007/s00376-017-7133-z.

McPhaden, Michael J., Zebiak, Stephen E., and Glantz, Michael H. ENSO as an Integrating Concept in Earth Science. *Science*, 314(5806):1740–1745, 2006. ISSN 0036-8075. doi: 10.1126/science.1132588. URL https://science.sciencemag.org/content/314/5806/1740.

Newman, Matthew, Sardeshmukh, Prashant D., and Penland, Cécile. How Important Is Air–Sea Coupling in ENSO and MJO Evolution? *Journal of Climate*, 22(11):2958–2977, 2009. ISSN 0894-8755. doi: 10.1175/2008JCLI2659.1. URL https://doi.org/10.1175/2008JCLI2659.1.

NOAA Climate Prediction Center, National Weather Service (NOAA CPC). Description of Changes to Ocean Niño Index (ONI), 2020a. URL https://origin.cpc.ncep.noaa.gov/products/analysis_monitoring/ensostuff/ONI_change.shtml. Online, accessed 29-October-2020.

NOAA Climate Prediction Center, National Weather Service (NOAA CPC). Cold & Warm Episodes by Season, 2020b. URL https://origin.cpc.ncep.noaa.gov/products/analysis_monitoring/ensostuff/ONI_v5.php. Online, accessed 29-October-2020.

Park, W., Keenlyside, N., Latif, M., Ströh, A., Redler, R., Roeckner, E., and Madec, G. Tropical Pacific Climate and Its Response to Global Warming in the Kiel Climate Model. *Journal of Climate*, 22(1):71–92, 2009. ISSN 0894-8755. doi: 10.1175/2008JCLI2261.1. URL https://doi.org/10.1175/2008JCLI2261.1.

Penland, Cécile and Sardeshmukh, Prashant D. The Optimal Growth of Tropical Sea Surface Temperature Anomalies. *Journal of Climate*, 8(8):1999–2024, 1995. ISSN 0894-8755. doi: 10.1175/1520-0442(1995)008⟨1999:TOGOTS⟩2.0.CO;2. URL https://doi.org/10.1175/1520-0442(1995)008<1999:TOGOTS>2.0.CO;2.

Penland, Cecile. Random Forcing and Forecasting Using Principal Oscillation Pattern Analysis. *Monthly Weather Review*, 117(10):2165–2185, 1989. ISSN 0027-0644. doi: 10.1175/1520-0493(1989)117⟨2165:RFAFUP⟩2.0.CO;2. URL https://doi.org/10.1175/1520-0493(1989)117<2165:RFAFUP>2.0.CO;2.

Plesca, Elina, Grützun, Verena, and Buehler, Stefan A. How Robust Is the Weakening of the Pacific Walker Circulation in CMIP5 Idealized Transient Climate Simulations? *Journal of Climate*, 31(1):81–97, 2017. ISSN 0894-8755. doi: 10.1175/JCLI-D-17-0151.1. URL https://doi.org/10.1175/JCLI-D-17-0151.1.

Stevens, Bjorn, Giorgetta, Marco, Esch, Monika, Mauritsen, Thorsten, Crueger, Traute, Rast, Sebastian, Salzmann, Marc, Schmidt, Hauke, Bader, Jürgen, Block, Karoline, Brokopf, Renate, Fast, Irina, Kinne, Stefan, Kornblueh, Luis, Lohmann, Ulrike, Pincus, Robert, Reichler, Thomas, and Roeckner, Erich. Atmospheric component of the MPI-M Earth System Model: ECHAM6. *Journal of Advances in Modeling Earth Systems*, 5(2):146–172, 2013. doi: 10.1002/jame.20015. URL https://agupubs.onlinelibrary.wiley.com/doi/abs/10.1002/jame.20015.

United Kingdom Met Office (UK Met Office). What is an ensemble forecast?, 2020. URL https://www.metoffice.gov.uk/research/weather/ensemble-forecasting/what-is-an-ensemble-forecast. Online, accessed 29-Oktober-2020.

Vecchi, Gabriel A. and Wittenberg, Andrew T. El Niño and our future climate: where do we stand? *WIREs Climate Change*, 1(2):260–270, 2010. doi: 10.1002/wcc.33. URL https://onlinelibrary.wiley.com/doi/abs/10.1002/wcc.33.

World Climate Research Programme (WCRP). WCRP Coupled Model Intercomparison Project (CMIP), 2020. URL https://www.wcrp-climate.org/wgcm-cmip. Online, accessed 29-October-2020.

Model References

Bader, David C., Leung, Ruby, Taylor, Mark, and McCoy, Renata B. E3SM-Project E3SM1.0 model output prepared for CMIP6 CMIP 1pctCO2. Version 20191008, 2019. URL https://doi.org/10.22033/ESGF/CMIP6.4490.

Bethke, Ingo, Wang, Yiguo, Counillon, François, Kimmritz, Madlen, Fransner, Filippa, Samuelsen, Annette, Langehaug, Helene Reinertsen, Chiu, Ping-Gin, Bentsen, Mats, Guo, Chuncheng, Tjiputra, Jerry, Kirkevåg, Alf, Oliviè, Dirk Jan Leo, Seland, Øyvind, Fan, Yuanchao, Lawrence, Peter, Eldevik, Tor, and Keenlyside, Noel. NCC NorCPM1 model output prepared for CMIP6 CMIP 1pctCO2. Version 20190914, 2019. URL https://doi.org/10.22033/ESGF/CMIP6.10861.

Boucher, Olivier, Denvil, Sébastien, Caubel, Arnaud, and Foujols, Marie Alice. IPSL IPSL-CM6A-LR model output prepared for CMIP6 CMIP 1pctCO2. Version 20180727, 2018. URL https://doi.org/10.22033/ESGF/CMIP6.5049.

Cao, Jian and Wang, Bin. NUIST NESMv3 model output prepared for CMIP6 CMIP 1pctCO2. Version 20190703, 2019. URL https://doi.org/10.22033/ESGF/CMIP6.8709.

Danabasoglu, Gokhan. NCAR CESM2 model output prepared for CMIP6 CMIP 1pctCO2. Version 20190425, 2019a. URL https://doi.org/10.22033/ESGF/CMIP6.7497.

Danabasoglu, Gokhan. NCAR CESM2-WACCM model output prepared for CMIP6 CMIP 1pctCO2. Version 20190425, 2019b. URL https://doi.org/10.22033/ESGF/CMIP6.10028.

Dix, Martin, Bi, Doahua, Dobrohotoff, Peter, Fiedler, Russell, Harman, Ian, Law, Rachel, Mackallah, Chloe, Marsland, Simon, O'Farrell, Siobhan, Rashid, Harun, Srbinovsky, Jhan, Sullivan, Arnold, Trenham, Claire, Vohralik, Peter, Watterson, Ian, Williams, Gareth, Woodhouse, Matthew, Bodman, Roger, Dias, Fabio Boeira, Domingues, Catia, Hannah, Nicholas, Heerdegen, Aidan, Savita, Abhishek, Wales, Scott, Allen, Chris, Druken, Kelsey, Evans, Ben, Richards, Clare, Ridzwan, Syazwan Mohamed, Roberts, Dale, Smillie, Jon, Snow, Kate, Ward, Marshall, and Yang, Rui. CSIRO-ARCCSS ACCESS-CM2 model output prepared for CMIP6 CMIP 1pctCO2, Version 20191109, 2019. URL https://doi.org/10.22033/ESGF/CMIP6.4230.

EC-Earth Consortium (EC-Earth). EC-Earth-Consortium EC-Earth3-Veg model output prepared for CMIP6 CMIP 1pctCO2. Version 20190702, 2019. URL https://doi.org/10.22033/ESGF/CMIP6.4507.

Guo, Huan, John, Jasmin G, Blanton, Chris, McHugh, Colleen, Nikonov, Serguei, Radhakrishnan, Aparna, Rand, Kristopher, Zadeh, Niki T., Balaji, V, Durachta, Jeff, Dupuis, Christopher, Menzel, Raymond, Robinson, Thomas, Underwood, Seth, Vahlenkamp, Hans, Bushuk, Mitchell, Dunne, Krista A., Dussin, Raphael, Gauthier, Paul PG, Ginoux, Paul, Griffies, Stephen M., Hallberg, Robert, Harrison, Matthew, Hurlin, William, Malyshev, Sergey, Naik, Vaishali, Paulot, Fabien, Paynter, David J, Ploshay, Jeffrey, Reichl, Brandon G, Schwarzkopf, Daniel M, Seman, Charles J, Shao, Andrew, Silvers, Levi, Wyman, Bruce, Yan, Xiaoqin,

Zeng, Yujin, Adcroft, Alistair, Dunne, John P., Held, Isaac M, Krasting, John P., Horowitz, Larry W., Milly, P.C.D, Shevliakova, Elena, Winton, Michael, Zhao, Ming, and Zhang, Rong. NOAA-GFDL GFDL-CM4 model output 1pctCO2. Version 20180701, 2018. URL https://doi.org/10.22033/ESGF/CMIP6.8470.

Hajima, Tomohiro, Abe, Manabu, Arakawa, Osamu, Suzuki, Tatsuo, Komuro, Yoshiki, Ogura, Tomoo, Ogochi, Koji, Watanabe, Michio, Yamamoto, Akitomo, Tatebe, Hiroaki, Noguchi, Maki A., Ohgaito, Rumi, Ito, Akinori, Yamazaki, Dai, Ito, Akihiko, Takata, Kumiko, Watanabe, Shingo, Kawamiya, Michio, and Tachiiri, Kaoru. MIROC MIROC-ES2L model output prepared for CMIP6 CMIP 1pctCO2. Version 20190823, 2019. URL https://doi.org/10.22033/ESGF/CMIP6.5370.

Jungclaus, Johann, Bittner, Matthias, Wieners, Karl-Hermann, Wachsmann, Fabian, Schupfner, Martin, Legutke, Stephanie, Giorgetta, Marco, Reick, Christian, Gayler, Veronika, Haak, Helmuth, de Vrese, Philipp, Raddatz, Thomas, Esch, Monika, Mauritsen, Thorsten, von Storch, Jin-Song, Behrens, Jörg, Brovkin, Victor, Claussen, Martin, Crueger, Traute, Fast, Irina, Fiedler, Stephanie, Hagemann, Stefan, Hohenegger, Cathy, Jahns, Thomas, Kloster, Silvia, Kinne, Stefan, Lasslop, Gitta, Kornblueh, Luis, Marotzke, Jochem, Matei, Daniela, Meraner, Katharina, Mikolajewicz, Uwe, Modali, Kameswarrao, Müller, Wolfgang, Nabel, Julia, Notz, Dirk, Peters, Karsten, Pincus, Robert, Pohlmann, Holger, Pongratz, Julia, Rast, Sebastian, Schmidt, Hauke, Schnur, Reiner, Schulzweida, Uwe, Six, Katharina, Stevens, Bjorn, Voigt, Aiko, and Roeckner, Erich. MPI-M MPI-ESM1.2-HR model output prepared for CMIP6 CMIP 1pctCO2. Version 20190710, 2019. URL https://doi.org/10.22033/ESGF/CMIP6.6434.

Krasting, John P., John, Jasmin G, Blanton, Chris, McHugh, Colleen, Nikonov, Serguei, Radhakrishnan, Aparna, Rand, Kristopher, Zadeh, Niki T., Balaji, V, Durachta, Jeff, Dupuis, Christopher, Menzel, Raymond, Robinson, Thomas, Underwood, Seth, Vahlenkamp, Hans, Dunne, Krista A., Gauthier, Paul PG, Ginoux, Paul, Griffies, Stephen M., Hallberg, Robert, Harrison, Matthew, Hurlin, William, Malyshev, Sergey, Naik, Vaishali, Paulot, Fabien, Paynter, David J, Ploshay, Jeffrey, Schwarzkopf, Daniel M, Seman, Charles J, Silvers, Levi, Wyman, Bruce, Zeng, Yujin, Adcroft, Alistair, Dunne, John P., Dussin, Raphael, Guo, Huan, He, Jian, Held, Isaac M, Horowitz, Larry W., Lin, Pu, Milly, P.C.D, Shevliakova, Elena, Stock, Charles, Winton, Michael, Xie, Yuanyu, and Zhao, Ming. NOAA-GFDL GFDL-ESM4 model output prepared for CMIP6 CMIP 1pctCO2. Version 20180701, 2018. URL https://doi.org/10.22033/ESGF/CMIP6.8473.

NASA Goddard Institute for Space Studies (NASA/GISS). NASA-GISS GISS-E2.1G model output prepared for CMIP6 CMIP 1pctCO2. Version 20190815, 2018a. URL https://doi.org/10.22033/ESGF/CMIP6.6950.

NASA Goddard Institute for Space Studies (NASA/GISS). NASA-GISS GISS-E2.1G model output prepared for CMIP6 CMIP 1pctCO2. Version 20180905, 2018b. URL https://doi.org/10.22033/ESGF/CMIP6.6950.

NASA Goddard Institute for Space Studies (NASA/GISS). NASA-GISS GISS-E2.1G model output prepared for CMIP6 CMIP 1pctCO2. Version 20190702, 2018c. URL https://doi.org/10.22033/ESGF/CMIP6.6950.

NASA Goddard Institute for Space Studies (NASA/GISS). NASA-GISS GISS-E2.1H model output prepared for CMIP6 CMIP 1pctCO2. Version 20190403, 2019a. URL https://doi.org/10.22033/ESGF/CMIP6.6951.

NASA Goddard Institute for Space Studies (NASA/GISS). NASA-GISS GISS-E2-2-G model output prepared for CMIP6 CMIP 1pctCO2. Version 20191120, 2019b. URL https://doi.org/10.22033/ESGF/CMIP6.6952.

Park, Sungsu and Shin, Jihoon. SNU SAM0-UNICON model output prepared for CMIP6 CMIP 1pctCO2. Version 20190323, 2019. URL https://doi.org/10.22033/ESGF/CMIP6.7782.

Ridley, Jeff, Menary, Matthew, Kuhlbrodt, Till, Andrews, Martin, and Andrews, Tim. MOHC HadGEM3-GC31-LL model output prepared for CMIP6 CMIP 1pctCO2. Version 20190620, 2019a. URL https://doi.org/10.22033/ESGF/CMIP6.5788.

Ridley, Jeff, Menary, Matthew, Kuhlbrodt, Till, Andrews, Martin, and Andrews, Tim. MOHC HadGEM3-GC31-LL model output prepared for CMIP6 CMIP 1pctCO2. Version 20190821, 2019b. URL https://doi.org/10.22033/ESGF/CMIP6.5788.

Ridley, Jeff, Menary, Matthew, Kuhlbrodt, Till, Andrews, Martin, and Andrews, Tim. MOHC HadGEM3-GC31-LL model output prepared for CMIP6 CMIP 1pctCO2. Version 20190821, 2019c. URL https://doi.org/10.22033/ESGF/CMIP6.5788.

Rong, Xinyao. CAMS CAMS_CSM1.0 model output prepared for CMIP6 CMIP 1pctCO2. Version 20190708, 2019a. URL https://doi.org/10.22033/ESGF/CMIP6.9701.

Rong, Xinyao. CAMS CAMS_CSM1.0 model output prepared for CMIP6 CMIP 1pctCO2. Version 20190726, 2019b. URL https://doi.org/10.22033/ESGF/CMIP6.9701.

Seferian, Roland. CNRM-CERFACS CNRM-ESM2-1 model output prepared for CMIP6 CMIP for experiment 1pctCO2. Version 20181018, 2018a. URL https://doi.org/10.22033/ESGF/CMIP6.3714.

Seferian, Roland. CNRM-CERFACS CNRM-ESM2-1 model output prepared for CMIP6 CMIP for experiment 1pctCO2. Version 20181031, 2018b. URL https://doi.org/10.22033/ESGF/CMIP6.3714.

Seferian, Roland. CNRM-CERFACS CNRM-ESM2-1 model output prepared for CMIP6 CMIP for experiment 1pctCO2. Version 20181107, 2018c. URL https://doi.org/10.22033/ESGF/CMIP6.3714.

Seferian, Roland. CNRM-CERFACS CNRM-ESM2-1 model output prepared for CMIP6 CMIP for experiment 1pctCO2. Version 20190328, 2018d. URL https://doi.org/10.22033/ESGF/CMIP6.3714.

Seland, Øyvind, Bentsen, Mats, Oliviè, Dirk Jan Leo, Toniazzo, Thomas, Gjermundsen, Ada, Graff, Lise Seland, Debernard, Jens Boldingh, Gupta, Alok Kumar, He, Yanchun, Kirkevåg, Alf, Schwinger, Jörg, Tjiputra, Jerry, Aas, Kjetil Schanke, Bethke, Ingo, Fan, Yuanchao, Griesfeller, Jan, Grini, Alf, Guo, Chuncheng, Ilicak, Mehmet, Karset, Inger Helene Hafsahl, Landgren, Oskar Andreas, Liakka, Johan, Moseid, Kine Onsum, Nummelin, Aleksi, Spensberger, Clemens, Tang, Hui, Zhang, Zhongshi, Heinze, Christoph, Iversen, Trond, and Schulz, Michael. NCC NorESM2-LM model output prepared for CMIP6 CMIP 1pctCO2. Version 20190815, 2019. URL https://doi.org/10.22033/ESGF/CMIP6.7802.

Semmler, Tido, Danilov, Sergey, Rackow, Thomas, Sidorenko, Dmitry, Barbi, Dirk, Hegewald, Jan, Sein, Dmitri, Wang, Qiang, and Jung, Thomas. AWI AWI-CM1.1MR model output prepared for CMIP6 CMIP 1pctCO2. Version 20181218, 2018. URL https://doi.org/10.22033/ESGF/CMIP6.359.

Stouffer, Ronald. UA MCM-UA-1-0 model output prepared for CMIP6 CMIP 1pctCO2. Version 20190731, 2019. URL https://doi.org/10.22033/ESGF/CMIP6.8881.

Swart, Neil Cameron, Cole, Jason N.S., Kharin, Viatcheslav V., Lazare, Mike, Scinocca, John F., Gillett, Nathan P., Anstey, James, Arora, Vivek, Christian, James R., Jiao, Yanjun, Lee, Warren G., Majaess, Fouad, Saenko, Oleg A., Seiler, Christian, Seinen, Clint, Shao, Andrew, Solheim, Larry, von Salzen, Knut, Yang, Duo, Winter, Barbara, and Sigmond, Michael. CCCma CanESM5 model output prepared for CMIP6 CMIP 1pctCO2. Version 20190429, 2019. URL https://doi.org/10.22033/ESGF/CMIP6.3151.

Tang, Yongming, Rumbold, Steve, Ellis, Rich, Kelley, Douglas, Mulcahy, Jane, Sellar, Alistair, Walton, Jeremy, and Jones, Colin. MOHC UKESM1.0-LL model output prepared for CMIP6 CMIP 1pctCO2. Version 20190701, 2019a. URL https://doi.org/10.22033/ESGF/CMIP6.5792.

Tang, Yongming, Rumbold, Steve, Ellis, Rich, Kelley, Douglas, Mulcahy, Jane, Sellar, Alistair, Walton, Jeremy, and Jones, Colin. MOHC UKESM1.0-LL model output prepared for CMIP6 CMIP 1pctCO2. Version 20191009, 2019b. URL https://doi.org/10.22033/ESGF/CMIP6.5792.

Tang, Yongming, Rumbold, Steve, Ellis, Rich, Kelley, Douglas, Mulcahy, Jane, Sellar, Alistair, Walton, Jeremy, and Jones, Colin. MOHC UKESM1.0-LL model output prepared for CMIP6 CMIP 1pctCO2. Version 20190604, 2019c. URL https://doi.org/10.22033/ESGF/CMIP6.5792.

Tatebe, Hiroaki and Watanabe, Masahiro. MIROC MIROC6 model output prepared for CMIP6 CMIP 1pctCO2. Version 20181212, 2018. URL https://doi.org/10.22033/ESGF/CMIP6.5371.

Voldoire, Aurore. CMIP6 simulations of the CNRM-CERFACS based on CNRM-CM6-1 model for CMIP experiment 1pctCO2. Version 20180626, 2018. URL https://doi.org/10.22033/ESGF/CMIP6.3712.

Voldoire, Aurore. CNRM-CERFACS CNRM-CM6-1-HR model output prepared for CMIP6 CMIP 1pctCO2. Version 20191021, 2019. URL https://doi.org/10.22033/ESGF/CMIP6.3713.

Volodin, Evgeny, Mortikov, Evgeny, Gritsun, Andrey, Lykossov, Vasily, Galin, Vener, Diansky, Nikolay, Gusev, Anatoly, Kostrykin, Sergey, Iakovlev, Nikolay, Shestakova, Anna, and Emelina, Svetlana. INM INM-CM4-8 model output prepared for CMIP6 CMIP 1pctCO2. Version 20190530, 2019. URL https://doi.org/10.22033/ESGF/CMIP6.4928.

Wieners, Karl-Hermann, Giorgetta, Marco, Jungclaus, Johann, Reick, Christian, Esch, Monika, Bittner, Matthias, Legutke, Stephanie, Schupfner, Martin, Wachsmann, Fabian, Gayler, Veronika, Haak, Helmuth, de Vrese, Philipp, Raddatz, Thomas, Mauritsen, Thorsten, von Storch, Jin-Song, Behrens, Jörg, Brovkin, Victor, Claussen, Martin, Crueger, Traute, Fast, Irina, Fiedler, Stephanie, Hagemann, Stefan, Hohenegger, Cathy, Jahns, Thomas,

Kloster, Silvia, Kinne, Stefan, Lasslop, Gitta, Kornblueh, Luis, Marotzke, Jochem, Matei, Daniela, Meraner, Katharina, Mikolajewicz, Uwe, Modali, Kameswarrao, Müller, Wolfgang, Nabel, Julia, Notz, Dirk, Peters, Karsten, Pincus, Robert, Pohlmann, Holger, Pongratz, Julia, Rast, Sebastian, Schmidt, Hauke, Schnur, Reiner, Schulzweida, Uwe, Six, Katharina, Stevens, Bjorn, Voigt, Aiko, and Roeckner, Erich. MPI-M MPI-ESM1.2-LR model output prepared for CMIP6 CMIP 1pctCO2. Version 20190710, 2019. URL `https://doi.org/10.22033/ESGF/CMIP6.6435`.

Wu, Tongwen, Chu, Min, Dong, Min, Fang, Yongjie, Jie, Weihua, Li, Jianglong, Li, Weiping, Liu, Qianxia, Shi, Xueli, Xin, Xiaoge, Yan, Jinghui, Zhang, Fang, Zhang, Jie, Zhang, Li, and Zhang, Yanwu. BCC BCC-CSM2MR model output prepared for CMIP6 CMIP 1pctCO2. Version 20181015, 2018. URL `https://doi.org/10.22033/ESGF/CMIP6.2833`.

Yukimoto, Seiji, Koshiro, Tsuyoshi, Kawai, Hideaki, Oshima, Naga, Yoshida, Kohei, Urakawa, Shogo, Tsujino, Hiroyuki, Deushi, Makoto, Tanaka, Taichu, Hosaka, Masahiro, Yoshimura, Hiromasa, Shindo, Eiki, Mizuta, Ryo, Ishii, Masayoshi, Obata, Atsushi, and Adachi, Yukimasa. MRI MRI-ESM2.0 model output prepared for CMIP6 CMIP 1pctCO2. Version 20190904, 2019. URL `https://doi.org/10.22033/ESGF/CMIP6.5356`.

Zhang, Jie, Wu, Tongwen, Shi, Xueli, Zhang, Fang, Li, Jianglong, Chu, Min, Liu, Qianxia, Yan, Jinghui, Ma, Qiang, and Wei, Min. BCC BCC-ESM1 model output prepared for CMIP6 CMIP 1pctCO2. Version 20190726, 2019. URL `https://doi.org/10.22033/ESGF/CMIP6.2834`.

Ziehn, Tilo, Chamberlain, Matthew, Lenton, Andrew, Law, Rachel, Bodman, Roger, Dix, Martin, Wang, Yingping, Dobrohotoff, Peter, Srbinovsky, Jhan, Stevens, Lauren, Vohralik, Peter, Mackallah, Chloe, Sullivan, Arnold, O'Farrell, Siobhan, and Druken, Kelsey. CSIRO ACCESS-ESM1.5 model output prepared for CMIP6 CMIP 1pctCO2. Version 20191115, 2019. URL `https://doi.org/10.22033/ESGF/CMIP6.4231`.

Appendix

All supplementary material can be found at: `http://doi.org/10.5281/zenodo.4153740`
The material includes the plots of the Welch's periodograms and e-folding times derived from fitting LIMs to different sub-samples of the MPI-ensemble. It also includes the same plots derived from fitting LIMs to each of the 68 ensemble members individually.
Additionally, all scripts that have been used to process and analyse the data can be found there.

List of Abbreviations

CMIP Coupled Model Intercomparison Project

CMIP5 Coupled Model Intercomparison Project Phase 5

CMIP6 Coupled Model Intercomparison Project Phase 6

DECK Diagnostic, Evaluation and Characterization of Klima

EN El Niño

ENSO El Niño Southern Oscillation

EOF empirical orthogonal function

GCM General Circulation Model

LIM Linear Inverse Model

LN La Niña

MA moving average

ONI Ocean Niño Index

PC principle component

piControl pre-industrial control simulation

PSD power spectral density

SST sea surface temperature

1pctCO2 1 percent CO_2

List of Figures

List of Tables

Hiermit versichere ich an Eides statt, dass ich die vorliegende Arbeit im Studiengang Meteorologie B.Sc. selbstständig verfasst und keine anderen als die angegebenen Hilfsmittel – insbesondere keine im Quellenverzeichnis nicht benannten Internet-Quellen — benutzt habe. Alle Stellen, die wörtlich oder sinngemäß aus Veröffentlichungen entnommen wurden, sind als solche kenntlich gemacht. Ich versichere weiterhin, dass ich die Arbeit vorher nicht in einem anderen Prüfungsverfahren eingereicht habe und die eingereichte schriftliche Fassung der auf dem elektronischen Speichermedium entspricht.
Mit der Ausstellung der Arbeit in der Fachbibliothek bin ich einverstanden.

Fiona Fix

Datum, Ort, Unterschrift